Three-dimensional isogeometrically enriched finite elements for frictional contact and mixed-mode debonding

Callum J. Corbett, Roger A. Sauer[1]

Aachen Institute for Advanced Study in Computational Engineering Science (AICES), RWTH Aachen University, Templergraben 55, 52056 Aachen, Germany

---

Abstract

We present an isogeometric enrichment technique for three-dimensional finite element computations applied to frictional contact and mixed-mode debonding. This is an extension of previous work that focused on two-dimensional and frictionless problems. To offer a more complete view of the enriched element's performance, a comparison of the results to tri-variate isogeometric discretizations and standard Lagrangian elements is also included here. The enrichment is applied by discretizing parts of the surface that require higher accuracy with isogeometric basis functions, while the rest of the body uses Lagrangian shape functions. By using an isogeometric surface representation, the higher continuity across element boundaries and higher order of interpolation can be exploited. At the same time, the generation of tri-variate isogeometric meshes is avoided.

A convergence study without any surface effects, involving only volume integrals, shows that the enriched elements can also be beneficial for these problems. The major advantage of the isogeometric element enrichment over standard tri-linear elements is demonstrated in contact problems including normal and tangential tractions. For both, mixed-mode cohesive debonding and frictional contact, the enrichment increases robustness and leads to more accurate results than standard linear Lagrangian elements. All computations are also compared to results using tri-variate isogeometric discretizations to give a complete picture of the element's performance. It is also shown that the proposed enrichment formulation has advantages in mesh generation.

Keywords: computational contact mechanics, isogeometric analysis, nonlinear finite element methods, cohesive zone modeling, peeling, friction

---

1 Introduction

The accurate description of surface effects and the computation of surface quantities can play a crucial role in engineering applications. In contact computations for instance, the contact pressure or quantities derived from contact forces are often of special interest. Besides accuracy and efficiency, also the robustness of such computations can be a critical aspect. This work aims at combining high surface accuracy with an efficient and simple bulk description. To

---

achieve this goal, the surface or parts of the surface that require high accuracy are discretized using isogeometric basis functions, while the rest uses standard Lagrangian finite elements. Isogeometric basis functions, like NURBS or T-splines, offer a higher order of interpolation and in general continuity of C^1 or higher across element boundaries. By applying the isogeometric enrichment only locally where it is required, the overall computational cost is only increased slightly, while the advantages of the method are available at the same time.

This has been shown in 2D and for three-dimensional frictionless normal contact in Corbett and Sauer (2014) and for enrichments involving higher-order Lagrangian and Hermite interpolation on the surface in Sauer (2011) and Sauer (2013). The isogeometric enrichment technique leads to major improvements in reaction forces and bending moments compared to standard linear Lagrange elements in sliding and peeling contact computations. In 2D, Hermite interpolation on the surface leads to solutions of comparable accuracy, but an extension to 3D does not exists. For the three-dimensional example considered in Corbett and Sauer (2014), the use of isogeometrically enriched elements leads to more accurate results while reducing the runtime by 35% compared to linear elements due to a reduction of the required number of Newton iteration steps.

Based on these promising results, this work extends the previous work by evaluating the general performance of the three-dimensional isogeometrically enriched elements in a convergence study. Also, the use of isogeometrically enriched elements in tangential contact is analyzed and discussed. The model problems are a debonding simulation using a mixed-mode exponential cohesive zone model and a frictional contact simulation using a stick-slip algorithm. A further novelty is the comparison of the enriched elements to tri-variate isogeometric finite elements. This extension offers a more complete picture of the performance of the enrichment technique, which has previously only been compared to tri-linear Lagrangian finite elements and other enrichment techniques. Furthermore, the enrichment of quadratic Lagrange element meshes is considered in addition to the linear Lagrange case considered so far.

A thorough discussion of finite element enrichment, isogeometric analysis, and computational contact mechanics can be found in Corbett and Sauer (2014) and references therein. The following gives a brief introduction and names some recent advancements.

The concept of isogeometric analysis (IGA) was introduced by Hughes et al. (2005) and has since been adopted in many fields. Originally, isogeometric analysis was developed to bridge the gap between computer aided design (CAD) and finite element analysis (FEA) and has become popular due to its advantageous approximation properties. In computational contact mechanics the use of IGA offers advantages due to the continuous surface representation and its basis functions, which are greater or equal to zero[3]. Continuity of C^1 or higher restricts the need to treat edge and corner contact to truly geometric features as opposed to edges and corners appearing as the result of a faceted C^0 discretization. Recent advances in computational contact with IGA include multiscale thermomechanical contact Temizer (2014), large deformation contact using T-splines Dimitri et al. (2014a), thermomechanical Mortar contact Dittmann et al. (2014), isogeometric collocation for contact De Lorenzis et al. (2015), and modeling of solid and liquid membrane contact Sauer et al. (2014) and Sauer (2014).

The construction of volumetric spline meshes is challenging due to the tensor-product nature of the basis that requires hexahedral meshing. Current research explores the mapping to polycubes Escobar et al. (2011), Wang et al. (2013), and Liu et al. (2014) or the use of immersed boundary meshes within the finite cell method Schillinger et al. (2012). The presented enrichment technique only requires an isogeometric surface representation and avoids the issue of

---

[3]Quadratic Lagrange basis functions for example also have negative values. Interpolating a positive value at such a position leads to a negative nodal contribution and can lead to an unphysical solution.

volumetric IGA meshes. This is achieved by connecting the isogeometric surface mesh with a standard Lagrangian finite element volume mesh which can be generated using widely available and existing meshing tools.

Isogeometric analysis has been used with cohesive zone models by Verhoosel et al. (2011) with NURBS and T-splines in 2D, by Corbett and Sauer (2014) for 2D NURBS-enriched elements, and by Dimitri et al. (2014b) with NURBS and T-splines in 2D and 3D. Within this work, three-dimensional isogeometrically enriched elements will be analyzed and compared to NURBS and Lagrangian solutions.

The following section 2 gives a brief overview of the theoretical background of the finite element set-up, IGA, and the contact models used within this work. The procedure of creating volumetric meshes from an isogeometric surface description is described in section 3. It is followed by an investigation of the enriched elements and their convergence behavior in section 4. Three numerical examples, comparing the enriched elements to fully Lagrangian and fully isogeometric elements are discussed in section 5. Section 6 summarized the results of the presented work.

2 Theory

This section presents the isogeometric enrichment technique and gives a brief overview of the contact formulations used in the numerical examples in section 5. The enrichment formulation is presented in a general, three-dimensional form. It can be applied to any finite element basis that admits a Bézier representation, including B-splines, NURBS, and T-splines, and is independent of the order of interpolation of the enrichment. The tangential contact formulations considered are frictional contact and a mixed-mode exponential cohesive zone model.

2.1 Finite element framework

In the following, two deformable bodies $\mathcal{B}_k$ $(k = 1, 2)$ in $\mathbb{R}^3$ are considered within the framework of large deformations. The weak form of the two-body system

$$\sum_{k=1}^{2} \left[\int_{\mathcal{B}_k} \mathrm{grad}(\delta\boldsymbol{\varphi}_k) : \boldsymbol{\sigma}_k \ \mathrm{d}v_k - \underbrace{\int_{\partial_c\mathcal{B}_k} \delta\boldsymbol{\varphi}_k \cdot \boldsymbol{t}_{ck} \ \mathrm{d}a_k}_{\text{virtual contact work}} - \delta\Pi_{\mathrm{ext},k} \right] = 0 \ , \quad \forall \ \delta\boldsymbol{\varphi}_k \in \mathcal{V}_k \tag{1}$$

is solved for the unknown deformation field $\boldsymbol{\varphi}_k \in \mathcal{U}_k$, where $\mathcal{U}_k$ is a suitable space for the deformation field. Within Eq. (1), $\boldsymbol{\sigma}_k$ is the Cauchy stress tensor, $\boldsymbol{t}_{ck}$ is the contact traction on surface $\partial_c\mathcal{B}_k$, $\delta\Pi_{\mathrm{ext},k}$ is the external virtual work, and $\mathcal{V}_k$ is the space of kinematically admissible variations. Dropping the index k for body $\mathcal{B}_k$, the contact traction

$$\boldsymbol{t}_c = \boldsymbol{t}_n + \boldsymbol{t}_t \tag{2}$$

can be decomposed into a normal component $\boldsymbol{t}_n$ and a tangential component $\boldsymbol{t}_t$.

A physical point $\boldsymbol{x}$ of body $\mathcal{B}_k$ is described by the mapping

$$\boldsymbol{x} = \boldsymbol{x}(\xi, \eta, \zeta) \quad \{\xi, \eta, \zeta\} \in \mathcal{P}^3 \tag{3}$$

which maps a point from the parametric space $\mathcal{P}^3$ to the physical space. On the surface $\partial\mathcal{B}_k$, a point is mapped from the 2D parameter space $\mathcal{P}^2$ to the 3D physical space by means of

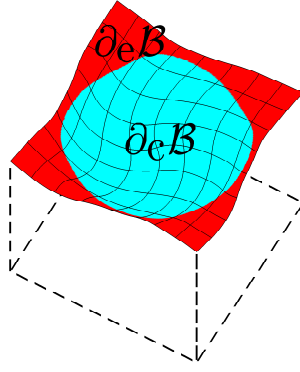$$\boldsymbol{x} = \boldsymbol{x}(\xi, \eta) \quad \{\xi, \eta\} \in \mathcal{P}^2 \ . \tag{4}$$

3

Figure 1: Schematic sketch of a body with an enriched surface $\partial_e \mathcal{B}$. The contact area $\partial_c \mathcal{B}$ is completely embedded within the enriched area.

In the discrete setting, denoted by a superscript h, each body is approximated such that $\mathcal{B}_k^h \approx \mathcal{B}_k$. This is done with a set of shape functions $\mathbf{N}$ and a set of discrete points $\mathbf{x}$, finite element nodes in traditional FE and control points in IGA. A point $\boldsymbol{x} \in \mathcal{B}_k$ is interpolated as

$$\boldsymbol{x} \approx \boldsymbol{x}^h = \mathbf{N}\mathbf{x} \tag{5}$$

with $\boldsymbol{x}^h \in \mathcal{B}_k^h$. Traditionally, Lagrange polynomials are used as shape functions for standard finite elements, although other choices are possible.

For problems dominated by effects on the surface or where surface quantities are of special interest, surface enrichment techniques can be applied. The presented surface enrichment technique describes the part of the surface that requires higher accuracy

$$\partial_e \mathcal{B}_k \subseteq \partial \mathcal{B}_k \tag{6}$$

using isogeometric basis functions, while the rest of the body can be discretized using standard Lagrangian finite elements. Note that the entire surface or only parts of it can be enriched. In the case of contact computations for instance, one would choose the enriched surface $\partial_e \mathcal{B}_k$ such that contact only occurs within this area,

$$\partial_c \mathcal{B}_k \subseteq \partial_e \mathcal{B}_k \,. \tag{7}$$

In Figure 1, a body $\mathcal{B}$ with an enriched surface $\partial_e \mathcal{B}$ is depicted. This area is chosen in such a way that the entire contact area $\partial_c \mathcal{B}$ is embedded within the enriched area.

In general, the contact area is not known a priori, which means that the enriched surface area must be chosen sufficiently large to cover all contact areas during the entire computation. Thus, enriching the surface adaptively only in the area currently needed is a promising approach for future research.

In order to introduce the enriched elements, first some concepts of IGA are presented in the following.

2.2 Isogeometric analysis

This section will focus on the key concepts necessary to understand and implement the isogeometrically enriched elements and will only give a brief overview. Details on the basics of

isogeometric analysis can be found in the literature, for instance in Hughes et al. (2005) and Cottrell et al. (2009), and will not be repeated here.

Using the Bézier extraction operator introduced in Borden et al. (2011) for NURBS and B-splines, and extended to T-splines in (Scott et al., 2011), the implementation of the enrichment is straightforward. A disadvantage of B-spline basis functions from a finite-element-implementation point of view is that they are in general different for each element. The localized Bézier extraction operator $\mathbf{C}^e$ allows B-spline basis functions $\hat{\mathbf{N}}^e = \{N_A^e\}_{A=1}^{p+1}$ of order p to be written as a linear combination of a set of Bernstein polynomials $\mathbf{B}^p = \{B_A^p\}_{A=1}^{p+1}$ for an element e. By expressing them in terms of Bernstein polynomials

$$\hat{\mathbf{N}}^e(\xi) = \mathbf{C}^e \mathbf{B}^p(\xi) \tag{8}$$

the function evaluation becomes the same for each element and can be precomputed at the quadrature points. The Bézier extraction operator $\mathbf{C}^e$ is in general different for each element, but it remains constant throughout the computation and only needs to be computed once.

For a two-dimensional surface, two Bézier extraction operators $\mathbf{C}_\xi^e$ and $\mathbf{C}_\eta^e$ and two sets of Bernstein polynomials $\mathbf{B}^p = \{B_A^p\}_{A=1}^{p+1}$ and $\mathbf{B}^q = \{B_A^q\}_{A=1}^{q+1}$ of order p and q in the direction of the parametric coordinates ξ and η, respectively, are required. The tensor product structure yields a set of

$$n_{\mathrm{cp}}^e = (p+1)(q+1) \tag{9}$$

B-spline basis functions $\hat{\mathbf{N}}^e = \{\hat{N}_A\}_{A=1}^{n_{\mathrm{cp}}^e}$, corresponding to the n_{cp}^e control points defining the element. The B-spline basis functions are given by

$$\hat{\mathbf{N}}^e(\xi, \eta) = \mathbf{C}_\xi^e \mathbf{B}^p(\xi) \otimes \mathbf{C}_\eta^e \mathbf{B}^q(\eta). \tag{10}$$

To go from B-spline basis functions to rational NURBS basis functions, a weight w_A is applied to each control point and corresponding basis function. With the weighting function

$$W(\xi, \eta) = \sum_{A=1}^{n_{\mathrm{cp}}^e} w_A \hat{N}_A^e(\xi, \eta) \tag{11}$$

the set of rational basis functions $\mathbf{R}^e = \{R_A^e\}_{A=1}^{n_{\mathrm{cp}}^e}$ is defined as

$$R_A^e(\xi, \eta) = \frac{w_A \hat{N}_A^e(\xi, \eta)}{W(\xi, \eta)}. \tag{12}$$

Using a tri-variate isogeometric discretization requires an additional Bézier extraction operator $\mathbf{C}_\zeta^e$ and set of Bernstein polynomials $\mathbf{B}^r = \{B_A^r\}_{A=1}^{r+1}$ of order r for the parametric ζ-direction. The number of control points and basis functions per element increases to

$$n_{\mathrm{cp,v}}^e = (p+1)(q+1)(r+1) \tag{13}$$

in the volumetric case. The B-spline basis functions $\hat{\mathbf{N}}_{\mathrm{v}} = \{\hat{N}_A\}_{A=1}^{n_{\mathrm{cp,v}}^e}$ are given by

$$\hat{\mathbf{N}}_{\mathrm{v}}(\xi, \eta, \zeta) = \mathbf{C}_\xi^e \mathbf{B}^p(\xi) \otimes \mathbf{C}_\eta^e \mathbf{B}^q(\eta) \otimes \mathbf{C}_\zeta^e \mathbf{B}^r(\zeta). \tag{14}$$

The extension to rational basis functions is equivalent to the two-dimensional case in Eq. (11) and Eq. (12).

Note that the generation of volumetric NURBS and T-spline meshes is challenging for general geometries and is a topic of current research, e.g. see Escobar et al. (2011), Wang et al. (2013),

Liu et al. (2014), and Schillinger et al. (2012). For the simple geometries considered in the scope of this work, the tri-variate meshes can be constructed manually and the results obtained with the tri-variate NURBS will be compared to those of the enriched elements. Only the case $p = q = r$ is considered, and the elements will be denoted IGAp, for instance IGA2 for quadratic NURBS in each parametric direction.

2.3 Isogeometric enrichment technique

The simplest three-dimensional isogeometrically enriched element is a tri-linear hexahedral element (denoted Q1), of which one surface is removed and replaced with an isogeometric discretization. This element will be used to introduce the enrichment technique. Instead of assuming that we begin with a volumetric mesh and replace part of the surface, the opposite point of view is more convenient and better reflects the actual workflow of mesh generation. To begin with, the isogeometric description of the surface $\partial\mathcal{B}_k$ is given. This automatically includes the discretization $\partial\mathcal{B}_k^h = \partial\mathcal{B}_k$ with Bézier surface elements, which live in the two-dimensional parametric space $\mathcal{P}^2$. From such a quadrilateral surface element, an enriched hexahedron is created by extending it in the parametric ζ-direction, e.g. using linear Lagrange shape functions and four finite element nodes. The surface $\zeta = -1$ is chosen as the enriched surface, without loss of generality. With Eq. (9) and Eq. (10), the set of $n_{\text{cp}} + 4$ element shape functions $\mathbf{N}^e = \{N_A\}_{A=1}^{n_{\text{cp}}+4}$ is then given by

$$
\begin{aligned}
N_1 &= R_1(\xi, \eta)\,\tfrac{1}{2}(1-\zeta) \\
N_2 &= R_2(\xi, \eta)\,\tfrac{1}{2}(1-\zeta) \\
&\vdots \\
N_{n_{\text{cp}}} &= R_{n_{\text{cp}}}(\xi, \eta)\,\tfrac{1}{2}(1-\zeta) \\
N_{n_{\text{cp}}+1} &= \tfrac{1}{8}(1-\xi)(1-\eta)(1+\zeta) \\
N_{n_{\text{cp}}+2} &= \tfrac{1}{8}(1+\xi)(1-\eta)(1+\zeta) \\
N_{n_{\text{cp}}+3} &= \tfrac{1}{8}(1+\xi)(1+\eta)(1+\zeta) \\
N_{n_{\text{cp}}+4} &= \tfrac{1}{8}(1-\xi)(1+\eta)(1+\zeta)\,.
\end{aligned}
\tag{15}
$$

The first n_{cp} shape functions are the combination of the Bézier surface quadrilateral with a linear interpolation in the third dimension, while the last 4 shape functions form the standard tri-linear Lagrangian basis. Partition of unity is fulfilled by construction. This is shown in the following section.

For the extension in the third dimension linear Lagrange interpolation can be considered in most cases in order to maintain the efficiency of the overall computation. However, as will be shown in the following finite element convergence study, the consideration of a quadratic extension using quadratic Lagrangian elements in the bulk domain is also possible, e.g. for cases where tri-linear elements suffer from shear locking. Although the computational cost of these elements is higher, they still offer the advantage of simpler mesh generation than tri-variate isogeometric meshes for general geometries while maintaining surface continuity. A schematic sketch of both, an enriched element with a linear and a quadratic extension in the ζ-direction, is shown in Figure 2.

The enriched elements with a quadratic Lagrangian extension are also briefly introduced. These elements offer higher accuracy and do not suffer from shear locking, but come at the cost of higher computational effort. The set of shape functions $N_i^{(2)}$ then consists of $n_{\text{cp}} + 18$ functions.
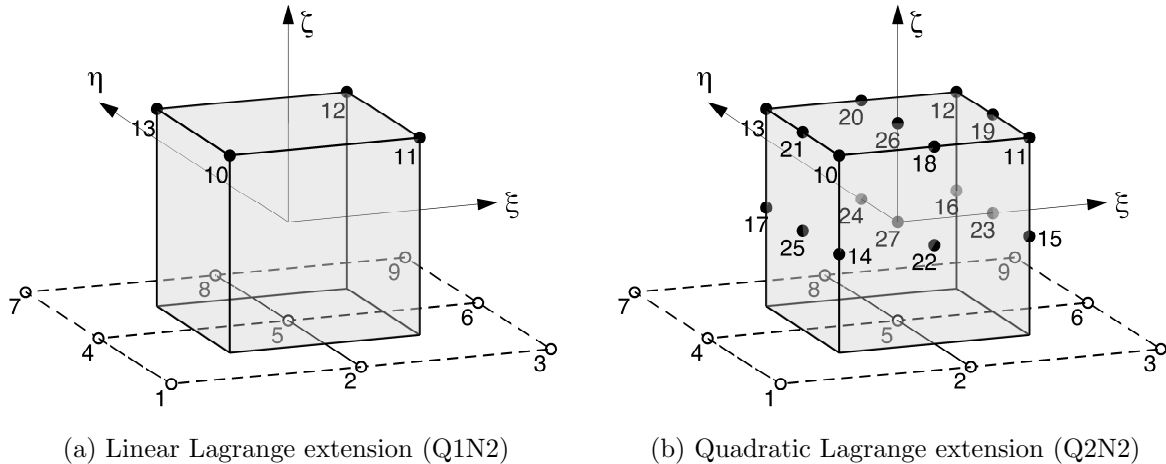
(a) Linear Lagrange extension (Q1N2) (b) Quadratic Lagrange extension (Q2N2)

Figure 2: Schematic sketch of elements with isogeometric surface enrichment.

Of these, the first n_{cp} functions

$$N_i^{(2)} = R_i(\xi, \eta) \, \frac{1}{2}(\zeta^2 - \zeta) \qquad i = 1, \ldots, n_{\mathrm{cp}} \tag{16}$$

form the enriched surface while the other 18 basis functions are the standard quadratic Lagrangian basis functions on the planes $\zeta = 0$ and $\zeta = 1$. These elements also form a partition of unity, shown in the following section. Figure 2b shows a schematic sketch of such an element.

In the examples in the following section, only the case $p = q$ for the degree of the isogeometric basis functions will be considered, although in general different orders may be chosen for each parametric direction. The enriched elements will be denoted Q1Np or Q2Np,where Q1 or Q2 denotes the Lagrangian base and Np the isogeometric surface of order p in each parametric direction. The letter N is chosen in accordance with Corbett and Sauer (2014) as an abbreviation of NURBS to avoid confusion of the number 1 and a capital I if isogeometric was used.

Figure 3 is a schematic sketch of different possibilities regarding surface discretization for the contact projection and the solution procedure. Different discretizations can be chosen for both operations, leading to the four cases considered here. We differentiate between faceted C^0 and smooth C^n with $n \geq 1$ meshes for both operations. The comparison clearly shows the difference between the standard linear Lagrange approach, surface smoothing techniques, and the proposed enrichment technique. In Figure 3 the solid black lines correspond to the finite element mesh used for analysis. The surface discretization used for the contact projection is shown as a dashed red line. The blue point is projected orthogonally onto the dashed surface mesh below. All meshes are created from the same geometry, but the schemes result in different distances and directions for the normal gap between the point and the surface. Using standard linear Lagrange elements, depicted in the upper left corner, both the geometry and the solution are C^0, so that the mesh for analysis and the mesh for the projection coincide. A surface smoothing technique like Bézier interpolation (see Wriggers (2008)) results in higher continuity on the surface mesh for the projection, the solution is nevertheless computed using the underlying C^0 elements. Also, the consistent linearization becomes increasingly complex, especially in the three dimensional case. This case is depicted in the upper right corner of Figure 3, the difference between the projection mesh (dashed line) and the analysis mesh (solid line) can be seen clearly. Using the proposed isogeometric enrichment technique, both the surface geometry and the solution have C^1 or higher continuity. There is no discrepancy between the surface used to compute the projection and the actual computational domain, as can be seen in the lower
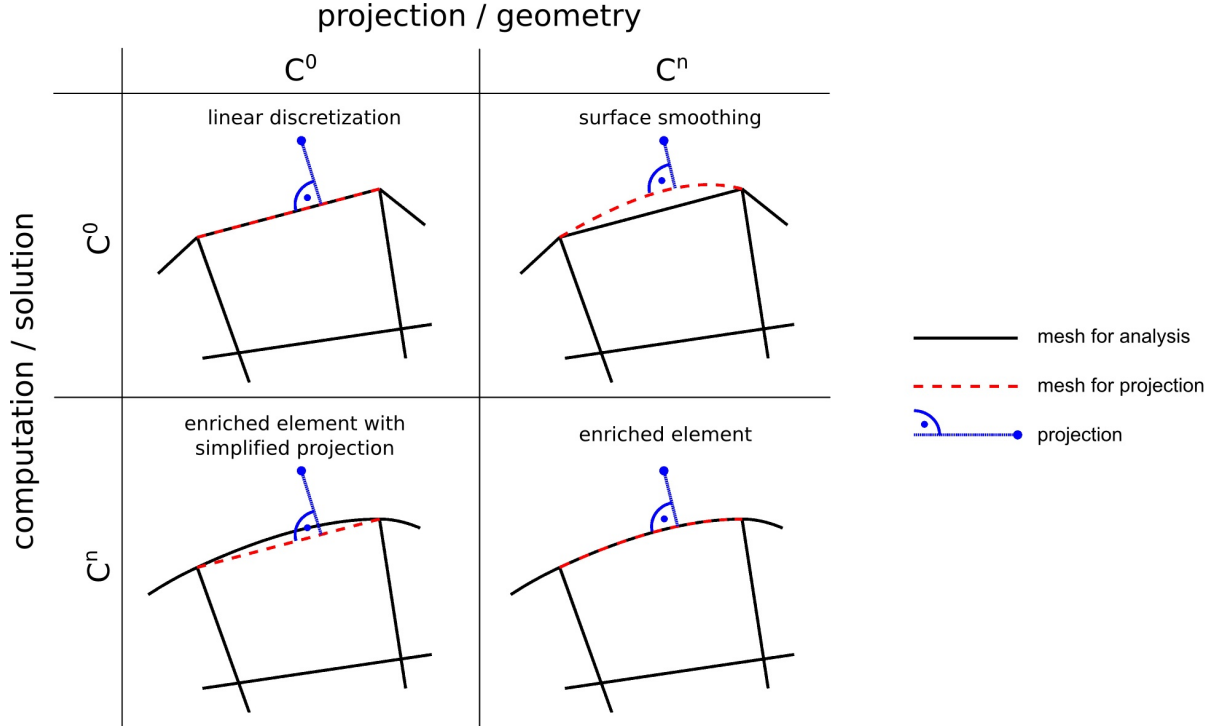
7

Figure 3: Comparison of the computation of the closest point projection using different discretization schemes.

right corner. For completeness, the case in the lower left corner is also included: it is possible to perform the computation on a smooth surface discretization while approximating the closest point projection with the linear interpolation of the surface. While reducing the computational effort for the projection, this re-introduces the problem of non-continuous normal vectors on the surface and thus is not considered a practical approach.

2.4   Partition of unity

To show that partition of unity is fulfilled for both the enrichment of linear and quadratic Lagrange elements, let $l_i(\xi)$ be the n_l one-dimensional Lagrange basis functions. In the linear case we have $n_l = 2$ basis functions

$$
\begin{aligned}
l_1(\xi) &= \frac{1}{2}\left(1 - \xi\right) \\
l_2(\xi) &= \frac{1}{2}\left(1 + \xi\right)
\end{aligned}
\tag{17}
$$

while the quadratic case leads to $n_l = 3$ basis functions

$$
\begin{aligned}
l_1(\xi) &= \frac{1}{2}\left(\xi^2 - \xi\right) \\
l_2(\xi) &= \frac{1}{2}\left(\xi^2 + \xi\right) \\
l_3(\xi) &= 1 - \xi^2\;.
\end{aligned}
\tag{18}
$$

For the proof we use the fact that both two-dimensional Lagrange basis functions and two-dimensional isogeometric basis functions form a partition of unity. We start with a tri-linear

Lagrange element, which also satisfies partition of unity. By pulling the surface at $\zeta = -1$ out of the sum and replacing it with the isogeometric discretization with n_{cp} basis functions we get

$$
\begin{aligned}
1 &= \sum_{i=1}^{n_l}\sum_{j=1}^{n_l}\sum_{k=1}^{n_l} l_i(\xi)\, l_j(\eta)\, l_k(\zeta) \\
&= \sum_{i=1}^{n_l}\sum_{j=1}^{n_l}\sum_{k=2}^{n_l} l_i(\xi)\, l_j(\eta)\, l_k(\zeta) \;+\; l_1(\zeta) \underbrace{\sum_{i=1}^{n_l}\sum_{j=1}^{n_l} l_i(\xi)\, l_j(\eta)}_{=1} \\
&= \sum_{i=1}^{n_l}\sum_{j=1}^{n_l}\sum_{k=2}^{n_l} l_i(\xi)\, l_j(\eta)\, l_k(\zeta) \;+\; l_1(\zeta) \underbrace{\sum_{i=1}^{n_{\mathrm{cp}}} R_i(\xi,\eta)}_{=1}\,.
\end{aligned}
\tag{19}
$$

In the last line of Eq. (19), the first term corresponds to the standard Lagrangian basis functions in the enriched element, while the second term sums up the mixed basis functions. With the total number of basis functions

$$
n_{\mathrm{no}} = n_{\mathrm{cp}} + n_l^2 \cdot (n_l - 1) = n_{\mathrm{cp}} + n_l^3 - n_l^2
\tag{20}
$$

we can then continue with

$$
\begin{aligned}
1 &= \sum_{i=1}^{n_l^3 - n_l^2} N_{n_{\mathrm{cp}}+i}(\xi,\eta,\zeta) \;+\; \sum_{i=1}^{n_{\mathrm{cp}}} N_i(\xi,\eta,\zeta) \\
&= \sum_{i=1}^{n_{\mathrm{no}}} N_i(\xi,\eta,\zeta)
\end{aligned}
\tag{21}
$$

where N_i are the enriched element's basis functions, see Eq. (15) and Eq. (16). The enrichment thus satisfies the partition of unity. Although we restrict ourselves to linear and quadratic Lagrange elements in the scope of this work, partition of unity is satisfied regardless of the degree of the Lagrangian base element.

2.5   Mesh refinement

Different options for mesh refinement have been discussed in detail in Corbett and Sauer (2014) and will be summarized here. The two methods used to refine NURBS patches are *order elevation* and *knot insertion*. Both methods can be repeated arbitrarily many times, but they are not commutative.

Using one quadratic line element with the knot vector $\Xi = [0\,0\,0\,2\,2\,2]$ this can be demonstrated. Inserting a unique knot leads to an additional element, while the order remains quadratic. The resulting knot vector is $\Xi = [0\,0\,0\,1\,2\,2\,2]$ and the continuity across the element border is C^1. Order elevation increases the order from p to $p+1$, but the continuity between existing knot spans is not increased. Applying order elevation to the original one-element curve results in a cubic curve with knot vector $\Xi = [0\,0\,0\,0\,2\,2\,2\,2]$.

Inserting a knot into this cubic curve leads to two cubic elements with C^2-continuity across the element border and the knot vector $\Xi = [0\,0\,0\,0\,1\,2\,2\,2\,2]$. This order of refinement was named k-refinement by Hughes et al. (2005). If on the other hand, order elevation is applied to the two-element quadratic curve, the two resulting elements are cubic but the continuity between

them remains only C^1. The corresponding knot vector is $\Xi = [0\,0\,0\,0\,1\,1\,2\,2\,2\,2]$. Note that the knot value 1 is repeated, leading to the reduced continuity between the elements.

Besides the difference in continuity, applying order elevation after knot insertion also leads to more control points, as can be seen by the length of the knot vector in the example above. The number of control points n_{cp} is given by

$$n_{\mathrm{cp}} = n_\Xi - (p+1) \tag{22}$$

where n_Ξ is the length of the knot vector. For computations dominated by effects on the surface, the additional degrees of freedom offered by these control points on the surface can be an advantage. Also, the basis span is reduced with respect to the element size, which is described in Corbett and Sauer (2014). This allows for a more accurate representation of sharp boundaries, which are otherwise smoothed by the large basis span of isogeometric basis functions. Due to this, the proposed refinement strategy to achieve a desired surface continuity, number of elements, and polynomial degree is the following:

1. start with the simplest surface representation possible

2. perform order elevation until the desired surface continuity is reached; the number of elements remains unchanged

3. insert unique knots until the desired number of elements is reached, leaving the order unchanged

4. perform t steps of additional order elevation to increase the polynomial degree and the number of control points on the surface while the number of elements and surface continuity remain unchanged

For $t = 0$ this results in standard k-refinement. For $t > 0$, the resulting elements will be denoted Q1N$p.t$ and Q2N$p.t$ for the linear and quadratic Lagrange case, respectively.

It is worth noting that the proposed additional order elevation leads to a large number of control points also in the volume when used with tri-variate isogeometric discretizations. Therefore, the advantage of this method could be canceled by the additional computational cost in this case. By restricting the isogeometric representation to the surface and using a Lagrangian basis in the bulk, the additional degrees of freedom are only created where they are needed and offer an advantage.

2.6   Normal contact

Here, normal contact is treated with the penalty method. In order to perform contact computations, the gap vector

$$\boldsymbol{g} = \boldsymbol{x}_k - \boldsymbol{x}_l \tag{23}$$

between two points $\boldsymbol{x}_k$ and $\boldsymbol{x}_l$ on neighboring surfaces $\partial\mathcal{B}_k$ and $\partial\mathcal{B}_l$, respectively, is required. In general, the minimum distance is obtained when $\boldsymbol{x}_l$ is chosen as the orthogonal projection of point $\boldsymbol{x}_k$ onto surface $\partial\mathcal{B}_l$. This projection point $\boldsymbol{x}_{\mathrm{p}} = \boldsymbol{x}_l(\xi_{\mathrm{p}}, \eta_{\mathrm{p}})$ is defined by the parametric coordinates ξ_{p} and η_{p} determined by a local Newton iteration. Note that this point is not necessarily unique and that in the case of a faceted surface, an orthogonal projection may not exist.

The distance between the surfaces is defined as

$$g = \begin{cases} -\|\boldsymbol{g}\|\,, & \text{if the surfaces penetrate} \\ \|\boldsymbol{g}\|\,, & \text{otherwise.} \end{cases} \tag{24}$$

To determine whether the surfaces penetrate, the normal gap

$$g_\mathrm{n} = (\boldsymbol{x}_k - \boldsymbol{x}_\mathrm{p}) \cdot \boldsymbol{n}_\mathrm{p} \tag{25}$$

with the surface normal $\boldsymbol{n}_\mathrm{p}$ at the projection point $\boldsymbol{x}_\mathrm{p}$ can be defined, which is negative if the bodies penetrate. A traction in normal direction, proportional to the penetration depth

$$\boldsymbol{t}_\mathrm{n}(\boldsymbol{x}_k) = \begin{cases} -\varepsilon_\mathrm{n}\, g_\mathrm{n}\, \boldsymbol{n}_\mathrm{p}, & g_\mathrm{n} < 0 \\ 0, & g_\mathrm{n} \geq 0 \end{cases} \tag{26}$$

is applied to each surface point in contact. For frictionless contact, the tangential traction $\boldsymbol{t}_\mathrm{t}$ is zero and the contact traction (Eq. (2)) simplifies to $\boldsymbol{t}_\mathrm{c} = \boldsymbol{t}_\mathrm{n}$[4].

The contact integrals are computed with the two-half pass algorithm by Sauer and De Lorenzis (2013), which evaluates the contact traction on each surface separately.

2.7 Frictional tangential contact

The theory for frictional contact can be found in computational contact textbooks like Laursen (2002) or Wriggers (2006). The implementation is based on the two-half-pass formulation of Sauer and De Lorenzis (2014), where further details can be found. Here, only a brief summary is provided. The frictional contact formulation uses a penalty regularization and is based on a classical predictor-corrector algorithm.

The tangential contact slip $\boldsymbol{g}_\mathrm{t}$ is decomposed into a reversible slip $\Delta\boldsymbol{g}_\mathrm{e}$ and an irreversible slip $\boldsymbol{g}_\mathrm{s}$. This decomposition

$$\boldsymbol{g}_\mathrm{t} = \boldsymbol{g}_\mathrm{s} + \Delta\boldsymbol{g}_\mathrm{e} \tag{27}$$

acts as a regularization for sticking.

Using Coulomb's law with the coefficient of friction μ and the contact pressure $p = \|\boldsymbol{t}_\mathrm{n}\|$, see Eq. (26), the tangential traction during sliding is

$$\boldsymbol{t}_\mathrm{t} = -\mu p \frac{\dot{\boldsymbol{g}}_\mathrm{t}}{\|\dot{\boldsymbol{g}}_\mathrm{t}\|} \tag{28}$$

with the relative tangential sliding velocity $\dot{\boldsymbol{g}}_\mathrm{t}$.

The slip criterion to distinguish between the stick and the slip case

$$\boldsymbol{f}_\mathrm{s} = \|\boldsymbol{t}_\mathrm{t}\| - \mu p \tag{29}$$

is used, where sticking occurs for $\boldsymbol{f}_\mathrm{s} < 0$ and sliding for $\boldsymbol{f}_\mathrm{s} = 0$. The contact traction $\boldsymbol{t}_\mathrm{c}$ is obtained by combining Eq. (26) and Eq. (28).

---

[4]The spacial traction $\boldsymbol{t}_\mathrm{n}$ is chosen over the usual nominal traction $\boldsymbol{T}_\mathrm{n}$ because it is needed in this form for the frictional case. The slight variational inconsistency that is introduced by this choice (see Stupkiewicz (2001)) only affects the tangent matrix and not the forces. This inconsistency vanishes as the penalty parameter goes to infinity and the penetration to zero.
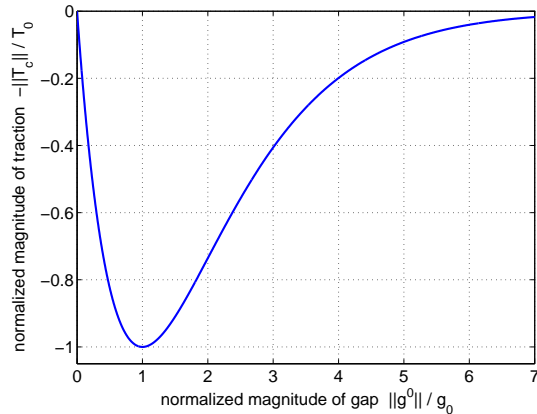
Figure 4: Magnitude of exponential cohesive zone traction over magnitude of gap, both normalized by the corresponding model parameter.

2.8 Cohesive zone modeling

To simulate the debonding of laminated material, cohesive zone models have been proposed. In the scope of this work, an exponential cohesive zone model based on Xu and Needleman (1993) is used. In the undeformed configuration, denoted by the superscript 0, each surface point $\boldsymbol{x}_k^0 \in \partial\mathcal{B}_k^0$ within the cohesive zone is projected onto the surface $\partial\mathcal{B}_l^0$. The parametric coordinates ξ_p^0 and η_p^0 of this projection point $\boldsymbol{x}_p = \boldsymbol{x}_l^0(\xi_p^0, \eta_p^0)$ are stored. Throughout the computation the gap vector defined in Eq. (23) is computed as the gap between the current surface point $\boldsymbol{x}_k$ and the current position of the original projection point, $\boldsymbol{x}_l(\xi_p^0, \eta_p^0)$. The gap vector will be denoted $\boldsymbol{g}^0$ to emphasize its relation to the reference configuration and set it apart from the gap vector used previously in normal contact and frictional contact.

Using the equality

$$\boldsymbol{t}_{ck}\, \mathrm{d}a_k = \boldsymbol{T}_{ck}\, \mathrm{d}A_k \tag{30}$$

the traction acting on surface $\partial\mathcal{B}_k$ can be expressed in terms of the reference surface rather than the current surface. Here, the traction on surface $\partial\mathcal{B}_k$ is given by the mixed-mode debonding law

$$\boldsymbol{T}_{ck}(\boldsymbol{x}_l) = -T_0\, \frac{\boldsymbol{g}^0}{g_0}\, \exp\left(1 - \frac{\|\boldsymbol{g}^0\|}{g_0}\right) \tag{31}$$

with the parameters T_0 and g_0. Figure 4 shows the magnitude of the exponential cohesive zone traction over the magnitude of the gap. The non-linearity, but also the smoothness of the function can clearly be seen. Also in this case, the two-half pass algorithm is used to evaluate the traction on each body separately.

Regarding penetration, the stiffness of the cohesive zone model can be too small and can lead to large penetrations. To avoid this, the cohesive zone model is coupled with a penalty approach according to Eq. (26)
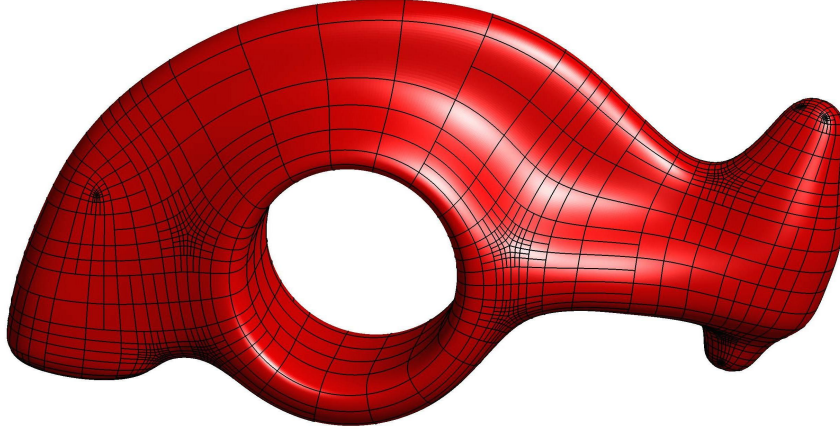
12

Figure 5: Simplified cubic T-spline surface mesh of a rocker arm.

2.9 Constitutive equation

Throughout this work, the hyperelastic Neo Hookean material model is used according to Zienkiewicz and Taylor (2005). The stress-strain relation for the Cauchy stress $\boldsymbol{\sigma}$ is

$$\boldsymbol{\sigma} = \frac{\Lambda}{J} \ln J \, \boldsymbol{I} + \frac{\mu}{J} \left(\boldsymbol{b} - \boldsymbol{I} \right) \tag{32}$$

with the determinant of the deformation gradient J, the identity tensor $\boldsymbol{I}$ and the left Cauchy–Green deformation tensor $\boldsymbol{b}$. The Lamé parameters μ and Λ can be expressed in terms of Young's modulus E and Poisson's ratio ν using

$$\mu = \frac{E}{2 \left(1 + \nu\right)} \qquad \text{and} \qquad \Lambda = \frac{2 \, \mu \, \nu}{1 - 2\nu} \; . \tag{33}$$

3 Volumetric meshing

Although tri-variate isogeometric mesh construction is possible, see for instance Escobar et al. (2011), Wang et al. (2013), or Liu et al. (2014), it is not widely available. Also, the higher polynomial degree and higher continuity may not be needed within the volume, in which case linear elements provide a computationally more efficient alternative. This section will outline how volumetric meshes can be created from a closed isogeometric surface using the proposed element enrichment technique.

To demonstrate the method a simplified model of a rocker arm will be used. The initial quadrilateral mesh was generated with the integer-grid map quad meshing algorithm by Bommes et al. (2013). Using this as input to the commercial CAD software Rhino with the T-spline plug-in, a T-spline surface can be created and exported. The Bézier elements of the resulting surface mesh are shown in Figure 5. For this demonstration, the entire surface is smooth with continuity of C^1 or higher. It is also possible to preserve sharp C^0 feature lines if desired.

To generate a mesh for the interior of the body, the corner points of each Bézier element are projected inwards along the normal vector of the surface. This is similar to the pillowing element layer used in Zhang et al. (2012), however here the inward projection is required to create hexagonal enriched elements with linear Lagrange shape functions in the third parametric direction. Here, a constant offset for the projection has been chosen for simplicity. The

(a) T-spline surface   (b) Isogeometrically enriched element layer   (c) Linear interior mesh with conforming surface   (d) Combined volumetric model
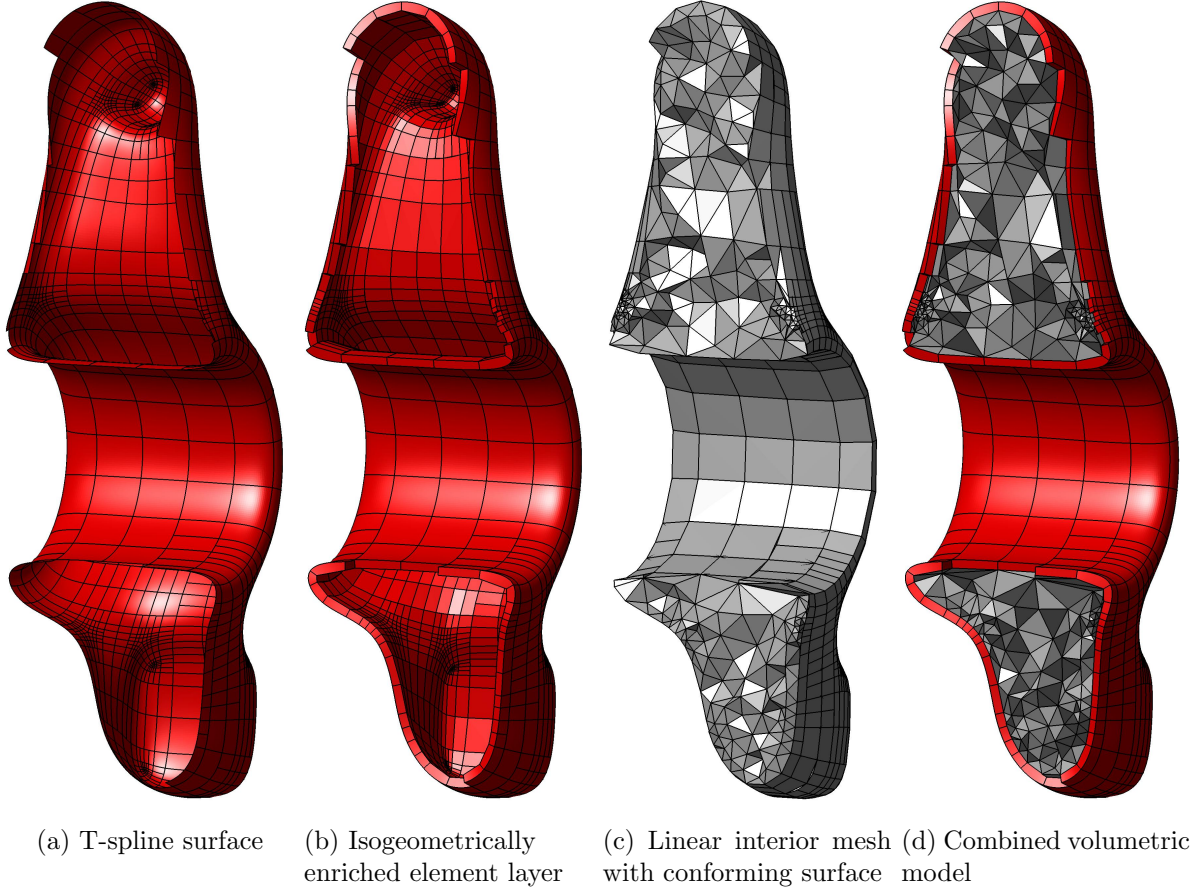
Figure 6: Generation of a volumetric mesh from a T-spline surface representation.

projection distance could however also be based on local features of the body. Figure 6a shows a cut through the exported surface mesh, Figure 6b shows the layer of enriched hexahedrons created by inward projection. The outer surface of this layer remains the exact same T-spline representation, while the inner surface consists of linear quadrilaterals.

Using this interior surface of linear quadrilaterals as input to commercial mesh generation software, a volumetric mesh can be constructed using pyramids and tetrahedral elements. The mesh is created in such a way that the surface mesh remains unchanged and thus conforms to the interior surface of the enriched element layer. This automatically generated volume mesh is shown in Figure 6c.

The last step of mesh generation consists of combining the outer layer of enriched elements with the interior mesh. The resulting mesh in Figure 6d shows a volumetric mesh using linear elements in the bulk and a T-spline representation on the surface.

When applying this method, T-junctions and extraordinary points on the surface do not require special attention as they are handled intrinsically by the T-spline representation. However, when projected inward while creating the enriched element layer, the T-junctions carry over to the linear interior mesh. In the finite element computation they can be dealt with for instance as hanging nodes. Regarding commercial mesh generation software, not all programs can deal with hanging nodes. To avoid this, one can resolve the issue in a pre-processing step by creating pyramids below the T-junctions, as depicted in Figure 7. Each quadrilateral element around the T-junction, depicted in gray in Figure 7a, forms the base of a pyramid. These pyramids all share one common node for their peak, shown in Figure 7b. The distance of the peak node

(a) T-spline surface (red) and linear base of enriched element layer (gray)

(b) Three pyramids with common peak node
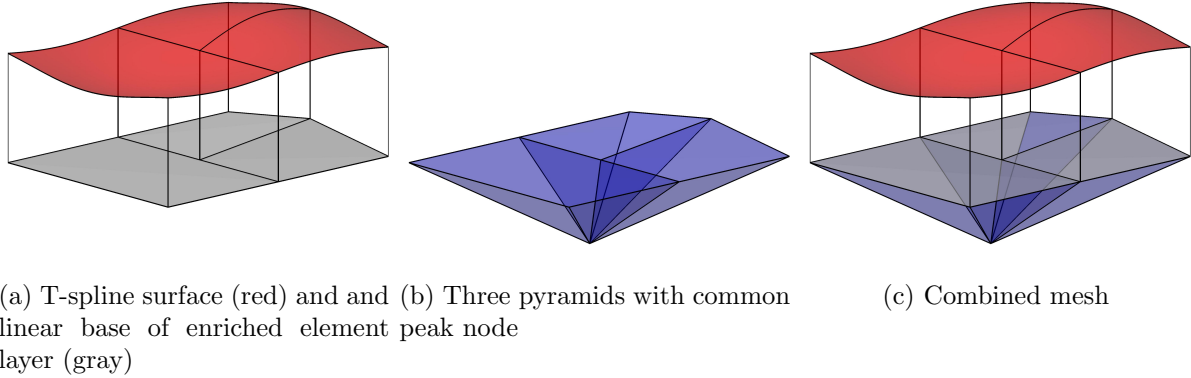
(c) Combined mesh

Figure 7: Pre-processing of T-junctions.

from the surface containing the T-junction can again be chosen based on local features of the geometry, but is considered constant here. Now, the seven outer faces of the pyramids can be passed to the mesh generator instead of the three quadrilaterals forming a T-junction. This way no hanging nodes are present in the input mesh of the mesh generation software. Extending this method one can also handle multiple T-junctions attached to the same element. Extraordinary points require no special treatment when creating an unstructured interior mesh.

4   A simple finite element convergence study

The general behavior of the three-dimensional isogeometrically enriched elements is studied in comparison with Lagrange and IGA discretizations in this section.

4.1   Problem set-up

Two benchmark problems are set-up. Both involve a solid cube with edge length L_0, which is compressed by 25% in the first case and stretched by 100% in the second case. The hyper-elastic Neo Hookean material model according to equation (32) is used with $\nu = 0.2$ and $E = 1E_0$. In both cases a displacement is applied to the nodes on the upper surface, which are fixed in the other directions. The base of the cube is completely fixed, so that the free faces of the cube form a convex or concave surface by bulging or necking, respectively. Using the symmetry of the system, only one fourth of the cube is modeled. Nested meshes are considered, with the coarsest mesh consisting of only two hexahedral elements with edge length $L_0/2$, see Figures 8 and 11. In the isogeometric case C^1 continuity is not enforced at the symmetry planes, so that the quarter model corresponds to a full model with C^0 continuity on the symmetry planes. Compared to the full model, the relative difference in the force is of the order 10^{-4} on the coarsest mesh and is reduced by more than an order of magnitude with each refinement step. The relative error due to the discretization is more than an order of magnitude larger, allowing for the quarter model without C^1 continuity to be used for the isogeometric cases without influencing the results negatively.

A variety of different element types are considered. To begin with, the cube is discretized using 8-node tri-linear Lagrange elements (Q1) and 27-node quadratic Lagrange elements (Q2). In the compressive case the tri-linear Lagrange elements are rather stiff, which is why the enhanced assumed strain (EAS) method introduced by Simo and Armero (1992) is used. These elements are enhanced with 9 extra modes and will be denoted Q1E9 elements. It is known that these

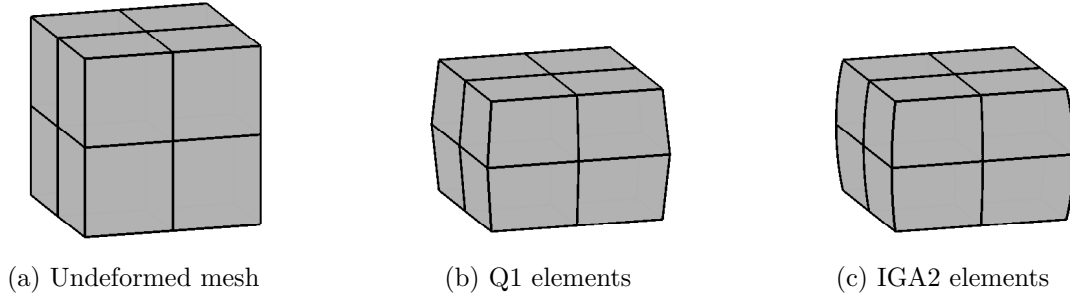(a) Undeformed mesh   (b) Q1 elements   (c) IGA2 elements

Figure 8: Coarsest full model for the compression test. Exploiting symmetry allows the use of only one quarter of the model.

elements can lead to hour-glassing when subjected to excessive compressive forces, see Wriggers (2008), which is not the case in the set-up considered here.

In the finite element model only two of the cube's faces are free to deform, while the other surfaces are subject to Dirichlet boundary conditions. The base is fixed, two sides are controlled by symmetry conditions, and the displacement of the top surface is prescribed. Of these two free surfaces, one or both may be enriched with a NURBS patch. Although it is possible to derive an element with two enriched sides, in a first approach this element proved quite stiff in both compression and tension. Due to this, in the case that both sides are enriched, the elements along the edge of the cube are split diagonally into two prisms with one enriched side each. In the current implementation, the prisms are modeled as degenerated hexahedra, although the derivation of isogeometrically enriched elements other than hexahedra, such as prisms, is possible.

In the following, the enriched meshes are denoted Q1N2, Q1E9+Q1N2, and Q2N2. The meshes denoted Q1E9+Q1N2 are constructed with Q1N2 element on one or both of the free surfaces and Q1E9 elements for the rest of the body. An isogeometrically enriched element with enhanced assumed strain, Q1E9N2, has not yet been developed. Additionally, a fully isogeometric discretization with quadratic NURBS is considered, denoted IGA2. For the convergence studies, a solution computed with fully isogeometric elements on a very fine mesh with approximately 1×10^6 degrees of freedom is used as a reference solution.

4.2 Evaluation of compression test

For the coarsest mesh, the undeformed and deformed configuration is shown in Figure 8 for tri-linear Lagrangian and isogeometric elements. The reaction force F_z in consequence of the compression is used as a quantity to measure the convergence of the different discretizations. Figure 9 shows the convergence of the reaction force F_z for the different element types with respect to the number of degrees of freedom. Even though the enhanced assumed strain elements have the same number of global degrees of freedom as the standard tri-linear elements, one must keep in mind that these elements come at a higher computational cost. For each element, static condensation is performed at the element level for the nine additional degrees of freedom.

First, we note that all element types converge to the same solution, which can be seen in Figure 9d. Only the element types Q1, Q1E9, Q2, and IGA2 are plotted here. The enriched elements lead to very similar results as can be seen by the convergence plots in Figure 9a - 9c. These are discussed in the following, and are omitted in Figure 9d for visibility. Regarding accuracy for a given number of degrees of freedom the fully isogeometric discretization and the

16

(a) Q1 series

(b) Q1E9 series
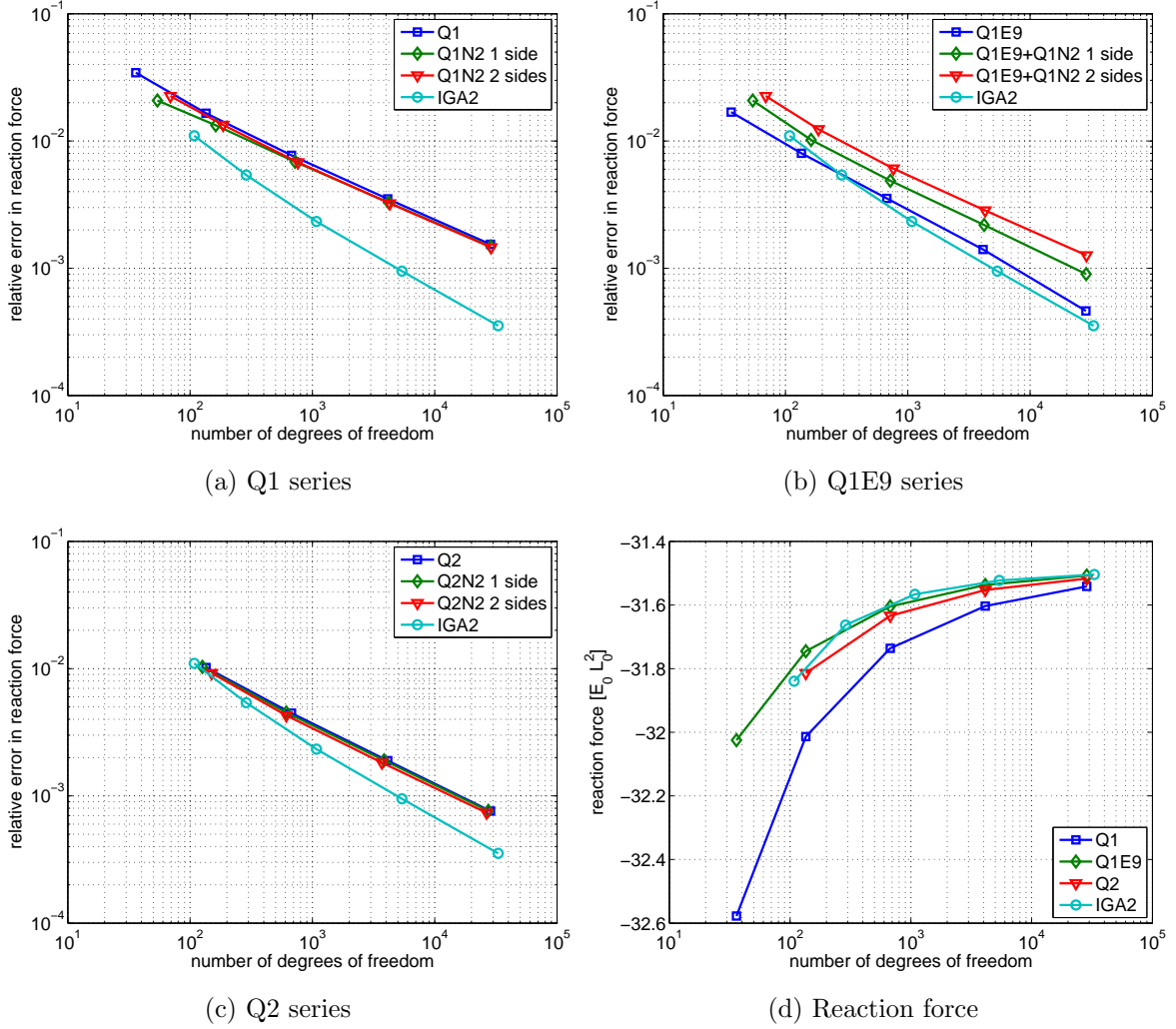
(c) Q2 series

(d) Reaction force

Figure 9: Convergence of reaction force F_z with respect to the number of degrees of freedom for compression, see Figure 8.

enhanced assumed strain elements offer the best performance. It should also be noted that the enhanced assumed strain elements even outperform the quadratic Lagrange elements.

Considering the enrichment of tri-linear (Q1) and quadratic (Q2) Lagrange elements in Figure 9a and 9c, one can see that the enrichment of the faces only increases the accuracy marginally. This result can be explained by the fact that only volume integrals are evaluated within the computation. The smooth surface description does not lead to a considerable advantage for this example.

For the enhanced assumed strain elements in Figure 9b, the enrichment of one or two faces even leads to worse results than the Q1E9 elements without enrichment. The EAS method is not applied to the layer of enriched elements which are based on the Q1 elements, which explains the stiffer behavior. Figure 10 shows the convergence of the Q1 and Q1E9 elements with and without one enriched side and that of the Q2 elements. Even though the relative error in the reaction force increases by adding an enriched element layer to the Q1E9 discretization, the result is still almost as good as that of the Q2 mesh. We believe that the extension of the enhanced assumed strain method to the isogeometrically enriched Q1N2 elements would lead to results as in the Q1 and Q2 cases, where the enrichment leads to slightly better results.
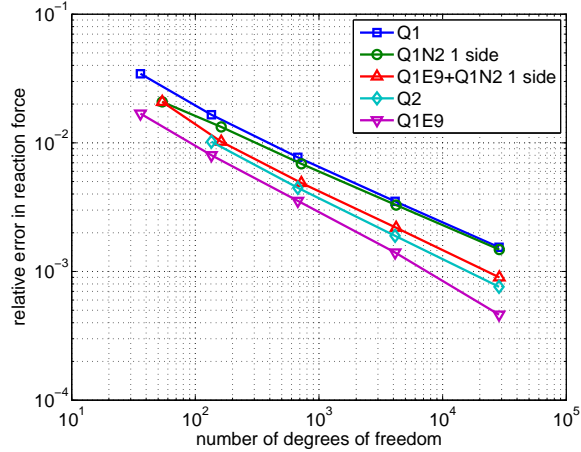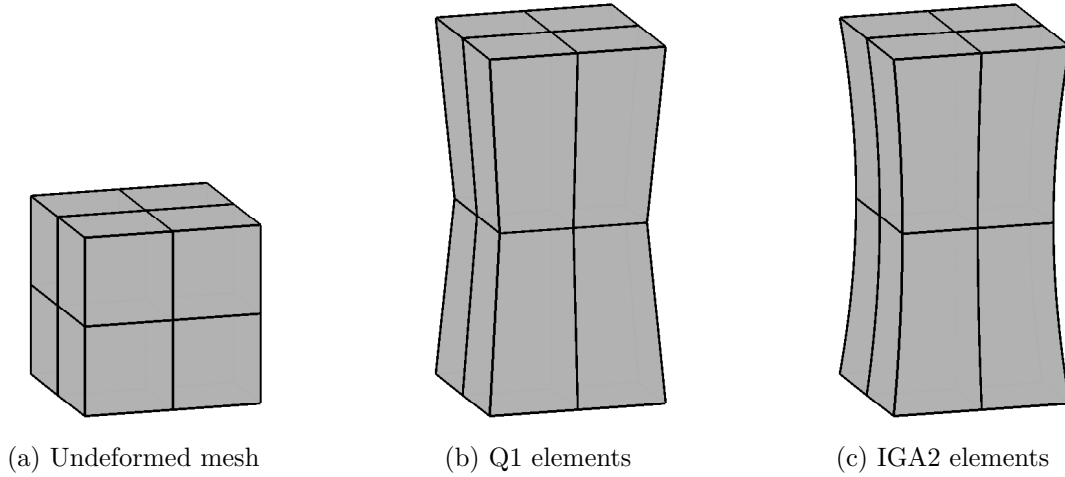
17

Figure 10: Influence of the isogeometric enrichment and the EAS method


(a) Undeformed mesh   (b) Q1 elements   (c) IGA2 elements

Figure 11: Coarsest full model for the extension test. Exploiting symmetry allows the use of only one quarter of the model.

4.3 Evaluation of extension test

As in the previous example, the reaction force F_z is used as a quantity to measure the convergence of the different discretizations. However, enhanced assumed strain elements Q1E9 are not considered in this case as the standard linear elements perform reasonably well. The undeformed and deformed configurations are shown in Figure 11 for tri-linear Lagrangian and isogeometric elements on the coarsest mesh. Figure 12a and 12b show the convergence of the reaction force F_z for linear and quadratic Lagrange elements with and without isogeometrically enriched sides and for tri-variate NURBS meshes with respect to the number of degrees of freedom. The force F_z is plotted with respect to the number of degrees of freedom in Figure 12d for Q1, Q1N2 on two sides, Q2, and IGA2 elements.

While the enrichment technique has a very slight negative influence on quadratic Lagrange elements Q2, the linear Lagrange elements Q1 benefit from the more accurate surface description. On coarse meshes, the relative error of linear Lagrange elements is reduced by a factor of approximately 2 with Q1N2 elements on one side, and approximately 3 with Q1N2 elements
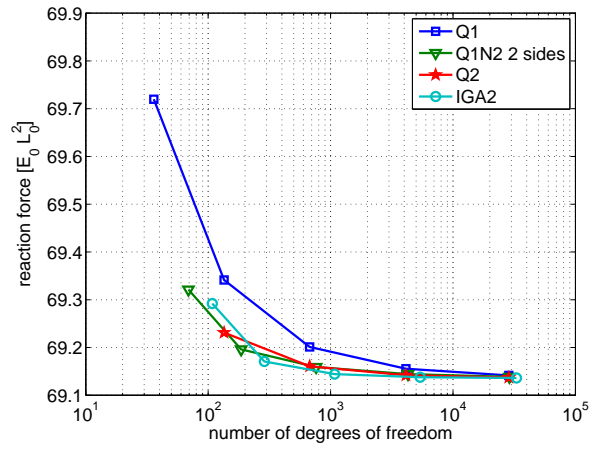
18
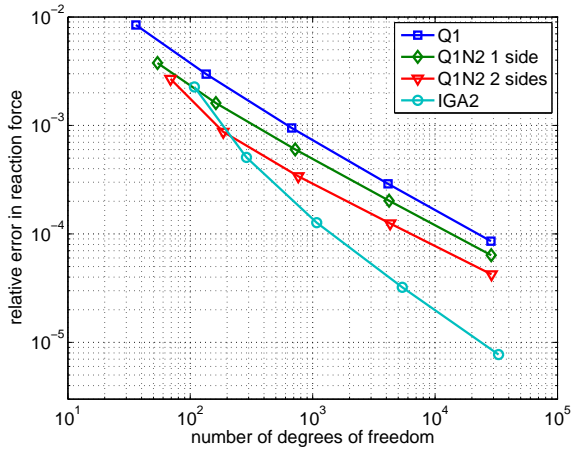
(a) Q1 series
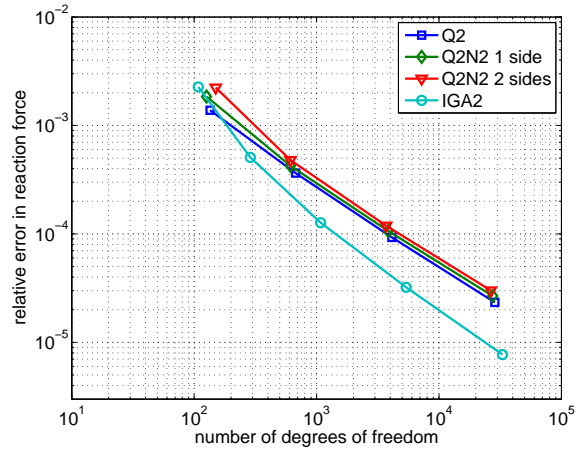
(b) Q2 series
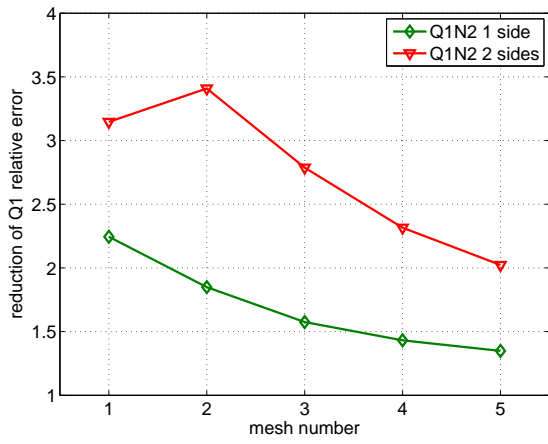
(c) Error reduction

(d) Reaction force

Figure 12: Convergence of reaction force F_z with respect to the number of degrees of freedom for tension.

on both sides. This substantial improvement can be seen in Figure 12c, where this factor is plotted with respect to the mesh number. The increase in degrees of freedom for the enriched elements is negligible due to the fact that the degrees of freedom in the volume increase with the power of 3, while the surface degrees of freedom only increase quadratically as the meshes are refined. With increasing mesh refinement, the improvement decreases, reaching 1.3 and 2.0 in this example.

4.4 Interpretation

The study shows that the enrichment of surfaces can lead to improvements in accuracy compared to standard linear Lagrange meshes, even when only volume integrals are considered. This is especially the case for coarse meshes. The large deformation in the extension test is captured more accurately by the isogeometrically enriched elements, leading to higher accuracy. However, in cases where finite element technology such as the enhanced assumed strain method is used to overcome an overly stiff element behavior, the results may worsen with Q1Np elements on the surface when only volume integrals are involved. It is emphasized that this is due to the linear Lagrange base of these elements, not the enrichment itself. The development of enriched elements with enhanced assumed strain, Q1E9Np elements, is a task for future research and could overcome these deficiencies in the volume-dominated case. In the following numerical examples that focus on the surface effects, the one layer of enriched elements has no deteriorative influence on the results.

One must also remember, that in the example at hand the mesh is very simple and a tri-variate, one-patch NURBS discretization exists. In general, the discretization of three-dimensional volumes by means of continuous isogeometric basis functions poses a challenge. In this case, one may only be able to resort to standard Lagrangian elements for the volumetric meshing, in which case the enriched elements pose a viable alternative. As long as no locking effects must be expected, Q1Np elements offer the most efficient option.

The enriched elements become more advantageous when a surface integral is involved. If one were for instance to replace the Dirichlet boundary condition on the upper surface with a prescribed normal surface pressure - a condition analogous to normal contact - the C^1-continuous surface representation of the enriched elements would prove beneficial and lead to more accurate results, as the following examples demonstrate.

5 Numerical contact and debonding examples

Three numerical examples are considered in this section. In all cases, the results of the isogeometrically enriched surface meshes (Q1Np) are compared to enhanced assumed strain tri-linear Lagrange finite element meshes (Q1E9) and to tri-variate NURBS meshes (IGAp). The first example examines mixed-mode debonding of two deformable, three-dimensional bodies. Frictionless sliding contact between two deformable, three-dimensional bodies is considered in the second example. In the third example, friction is added to the previous case, leading to tangential sticking and sliding contact in addition to normal contact.

5.1 Mixed-mode cohesive debonding

The debonding of two initially flat bodies, an elastic strip and an elastic plate, is considered, depicted in Figure 13. The upper strip $\mathcal{B}_1$ (with dimension $19.5L_0 \times 4L_0 \times 1L_0$) is rotated by
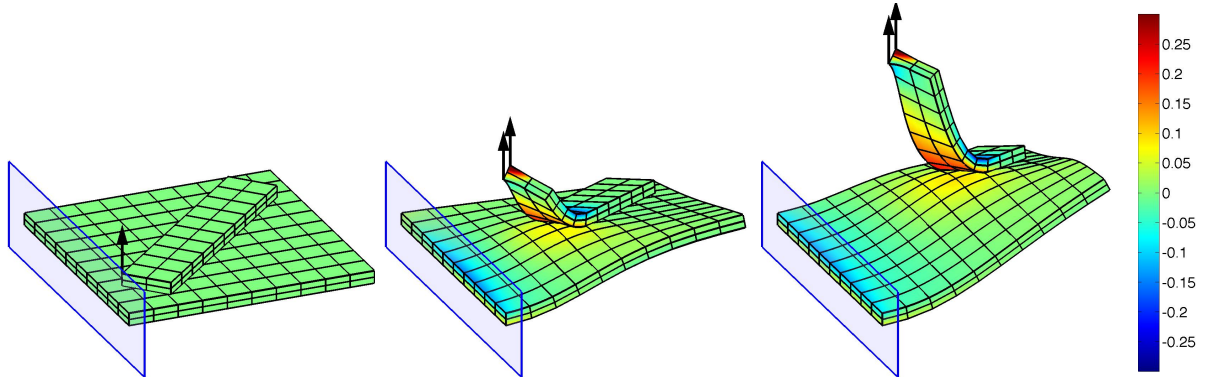
Figure 13: Set-up of the cohesive debonding problem and resulting deformation shown for the coarsest isogeometrically enriched mesh (Q1E9+Q1N2) for a prescribed vertical displacement of $0L_0$, $7.75L_0$, and $15.5L_0$. The coloring represents the first stress invariant $I_1 = \operatorname{tr}\boldsymbol{\sigma}/E_0$.

mesh	elements	
	$\mathcal{B}_1$	$\mathcal{B}_2$
1	$10 \times 2 \times 2$	$10 \times 10 \times 2$
2	$20 \times 4 \times 4$	$20 \times 20 \times 4$
3	$40 \times 8 \times 8$	$40 \times 40 \times 8$

Table 1: Number of elements in meshes used for the cohesive debonding problem.

$43°$ with respect to the lower plate $\mathcal{B}_2$ (with dimension $20L_0 \times 20L_0 \times 1L_0$) to create the general case of non-conforming meshes in the interface and an asymmetric set-up. Initially 21% of the interface is debonded, with the cohesive zone acting only on the rest of it. The parameters for the cohesive zone model in Eq. (31) are $g_0 = 0.08L_0$ and $T_0 = 0.1E_0$, with the parameters for length L_0 and stress E_0 normalizing the problem. At the initially debonded side, a vertical displacement is prescribed to an edge of the upper strip, while the lower strip is fully fixed along one side. The loading leads to a twisting motion during peeling and large deformation of both bodies, as Figure 13 shows. Hyperelastic material behavior according to the Neo-Hookean material model in Eq. (32) is considered for both bodies with $\nu = 0.3$. Young's modulus of the plate is $E_2 = E_0$, while the strip is three times as stiff with $E_1 = 3E_0$.

Due to the strong cohesive forces, the strips undergo torsion and large bending, leading to shear locking in the linear Lagrange elements. The fully isogeometric discretization on the other hand does not suffer from this drawback. To overcome locking, the enhanced assumed strain method by Simo and Armero (1992) is used for all tri-linear Lagrange elements. As has been discussed in the previous section, no treatment of shear locking has been developed for the layer of enriched elements yet. This results in some shear locking of these elements which is due to the linear Lagrangian part of the element, not the enrichment itself.

Three nested meshes are considered here, which are listed in Table 1. The number of degrees of freedom for the different discretizations is listed in Table 2. For each level of refinement, the number of degrees of freedom of the discretizations based on linear Lagrange elements and the purely isogeometric discretization is of approximately the same magnitude. The number of degrees of freedom increases drastically for the discretizations including quadratic Lagrange elements. For this reason, the values in parentheses refer to meshes for which no computation was performed.

To prevent the bodies from penetrating, a penalty method for normal contact with $\varepsilon_n = 10E_0/L_0^2$

mesh	number of degrees of freedom							
	Q1E9	Q1E9 +Q1N2	Q1E9 +Q1N3	Q1E9.1 +Q1N2.1	Q2	Q2N2	Q2N2.1	IGA2
1	1386	1500	1626	2772	8190	7128	8400	2304
2	8190	8400	8622	13104	55350	51048	55752	11088
3	55350	55752	56166	73800	(404838)	(387576)	(405624)	65520

Table 2: Degrees of freedom in meshes used for the cohesive debonding problem. No computation was performed for values in parentheses.
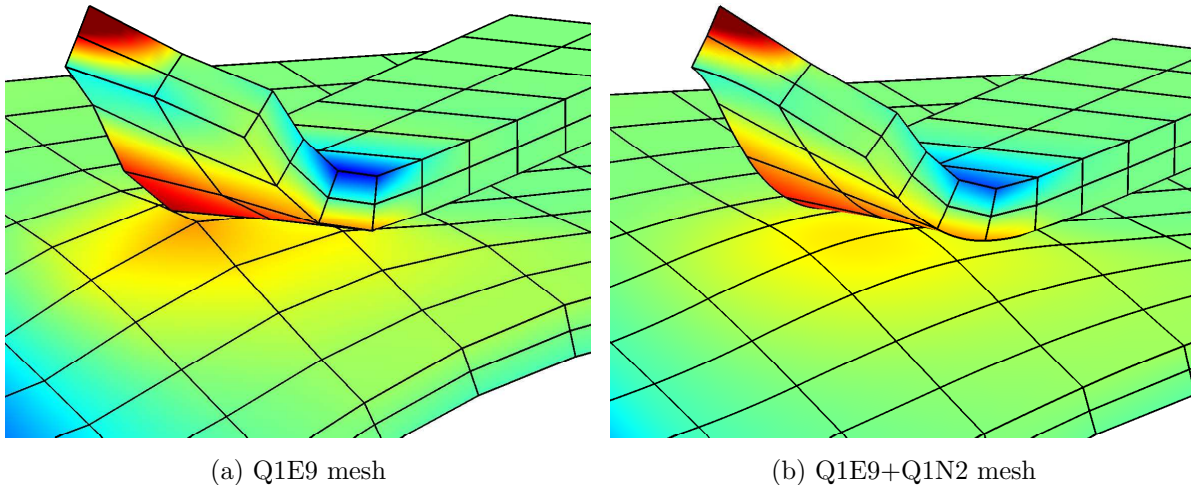

(a) Q1E9 mesh

(b) Q1E9+Q1N2 mesh

Figure 14: Comparison of the deformed surfaces at a prescribed displacement of $6.4L_0$ for mesh 1. The coloring is the same as in Figure 13

is applied to the elements in the interface additionally to the cohesive traction. The surface integrals, involving contributions from the exponential cohesive zone model and normal contact, are evaluated using 10×10 quadrature points on each surface element.

On the coarsest mesh all computations show high fluctuations in the peeling force and fail before the strips are completely debonded. The mesh is to coarse to capture the debonding law correctly, which leads to sudden, unstable debonding of individual surface elements[5]. With these coarse meshes however the difference between a linear surface representation and the isogeometric enrichment can clearly be seen. A close-up of the deformed surfaces during peeling is shown for a linear and an isogeometric surface description in Figure 14. The smooth cohesive forces according to Eq. (31) should also lead to a smooth deformation and stress field. However, on the faceted surface of the linearly meshed plate a peak stress value is clearly visible in the peeling front where the deformation cannot be captured accurately. In contrast, the isogeometric surface discretization results in both a smooth deformation and stress field.

For all element choices except for the tri-linear enhanced strain Q1E9 elements which fail, mesh 2 allows the computations to run until the strips are entirely debonded. This is shown in Figure 15a and shows the benefit of the smooth and higher order surface discretization of the enrichment. The reaction force still shows high fluctuations in all cases, which are only diminished to an acceptable level with mesh 3, as can be seen in Figure 15b. On this mesh, the force-displacement curves are almost indistinguishable, except for the small difference in the peak value between the purely isogeometric mesh and the other meshes, where some shear

---

[5]In order to continue quasi-static computations, arc-length methods are needed, see Crisfield and Alfano (2002)
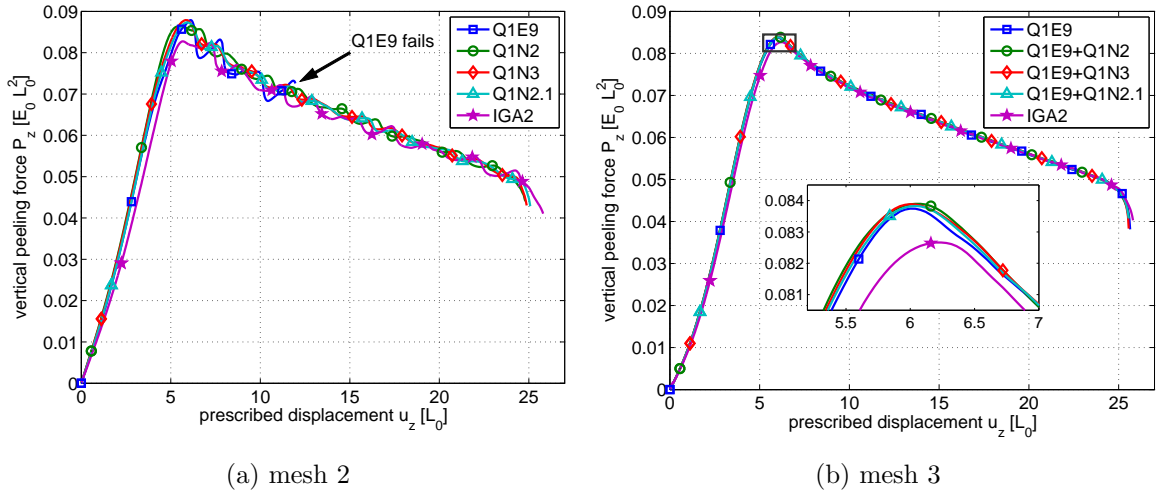
(a) mesh 2   (b) mesh 3

Figure 15: Peeling force for different element types.
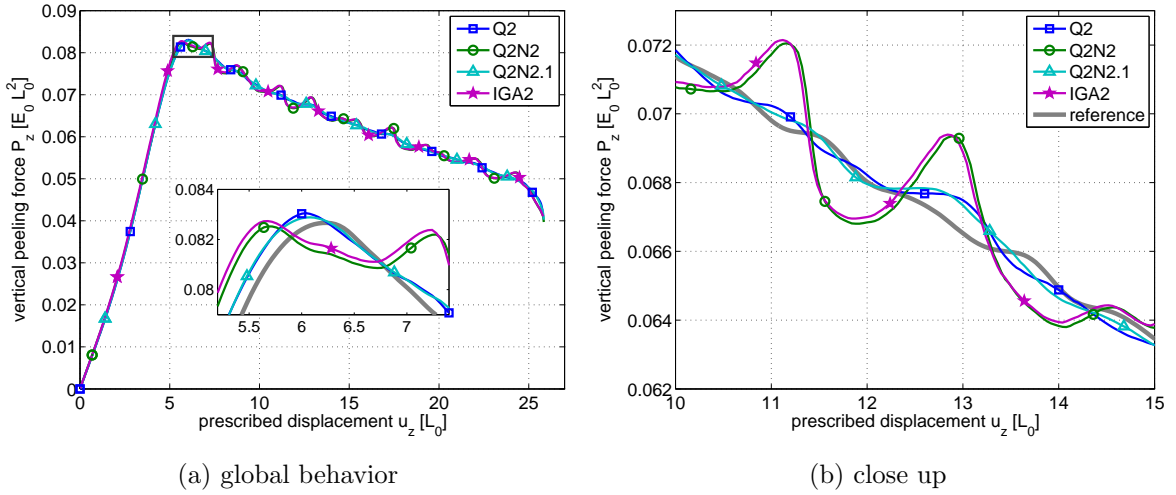

(a) global behavior   (b) close up

Figure 16: Peeling force for quadratic Lagrange elements on mesh 2.

locking is still present. It is worth noting that this also applies to the discretization using only enhanced assumed strain elements Q1E9, not only the enriched meshes.

To eliminate locking in these cases, quadratic Lagrange elements (Q2) can be used in the bulk and as the base element for the enrichment (Q2N2). By doing so, the resulting peeling forces of the quadratic isogeometric mesh IGA2 and the enriched elements Q2N2 become almost indistinguishable, as is shown in Figure 16 for mesh 2. These meshes use identical contact surface representations and only differ in the bulk. It should be noted that the discretizations using quadratic Lagrange elements require 4.6 to 5 times as many degrees of freedom as quadratic NURBS in this case, but offer simpler mesh generation for general geometries.

The gray reference line without any markers in Figure 16 is the purely isogeometric discretization on the next finer mesh, mesh 3. The total number of degrees of freedom is only slightly higher than that of the quadratic Lagrange discretizations on mesh 2. One can observe that the peeling problem depends very much on the number of degrees of freedom or respectively the number of nodes on the surface, summarized in Table 3 for a surface discretized by $n \times n$ elements. Using only quadratic Lagrange elements (Q2), the results are very similar to these obtained with the

23

element type	number of nodes
Q1	$(n+1)^2$
IGA2 / N2	$(n+2)^2$
Q2	$(2n+1)^2$
N2.1	$(2n+2)^2$

Table 3: Number of nodes for a surface discretized by $n \times n$ elements for different element types.
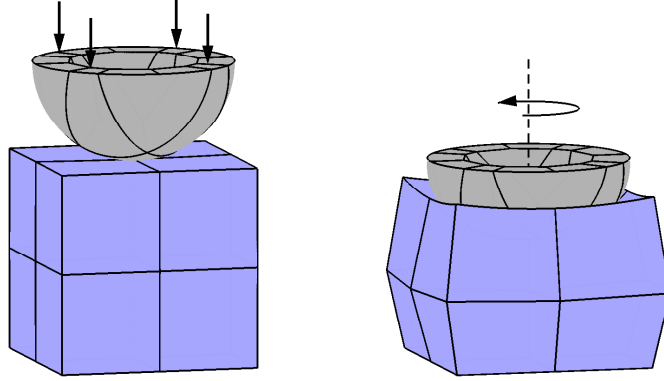

Figure 17: Set-up of both the frictionless and frictional sliding problem shown for the coarsest mesh.

Q2N2.1 meshes. The Q2N2.1 elements have a cubic NURBS surface, but are only C^1-continuous across element borders. They are created by order elevating the quadratic NURBS patch once after knots have been inserted to create the desired number of elements, see subsection 2.5. Both meshes, Q2 and Q2N2.1 have a similar amount of degrees of freedom on the contact surface. Because nested meshes are used, the reference line corresponds to an isogeometric discretization with twice as many elements in each dimension. Thus, regarding Table 3, the IGA2 mesh with $2n \times 2n$ elements on the surface has the same number of nodes on the surface as the Q2N2.1 discretization with $n \times n$ elements.

In summary, one can note that all isogeometric enrichments perform well in terms of reducing the reaction force oscillation, leading to a more robust computation than with linear Q1E9 elements. The additional computational cost is very low for Q1-based elements, as is shown in Table 2. However, all Q1E9-based meshes, also the Q1E9 meshes without enriched surfaces, suffer from some shear locking. For a given number of degrees of freedom, the IGA2, Q2, and Q2N2.1 meshes yield the best results for this example. The quadratic Lagrange elements Q2 have the drawback, that edge and corner contact must be treated in the penalty method used to avoid penetration, making it the least favorable of the three choices. For general geometries, a purely isogeometric mesh may not be available, in which case a Q2N2.1 mesh should be considered if shear locking is an issue.

5.2 Frictionless sliding contact

The problem set-up, depicted in Figure 17, is as follows: A vertical displacement is applied to the top of body $\mathcal{B}_1$, a thick, hollow hemisphere with radius L_0 and thickness $1/3 L_0$, which presses it into body $\mathcal{B}_2$, a cube with edge length $2L_0$ and a fixed base. Following the downward motion, a rotation of $180°$ is prescribed on the top of the hemisphere, leading to frictionless sliding

mesh	ε_{n}	elements		Q1E9	Q1E9 +Q1N2	Q1E9 +Q1N3	Q1E9 +Q1N2.1	IGA2
	$[E_0/L_0^2]$	$\mathcal{B}_1$	$\mathcal{B}_2$					
1	125	$3 \times 3 \times 1$	$2 \times 2 \times 2$	177	225	285	402	417
2	250	$7 \times 7 \times 2$	$4 \times 4 \times 4$	951	1035	1131	1752	1620
3	500	$11 \times 11 \times 3$	$8 \times 8 \times 8$	3915	4047	4191	5940	5535

Table 4: Meshes used for the sliding contact problems.

between the two bodies. The Neo-Hookean material according to Eq. (32) with $\nu = 0.3$ and $E_1 = 5E_0$ for the hemisphere and $E_2 = E_0$ for the cube is used. Normalization of the problem is thus achieved with the length L_0 and pressure E_0. Normal contact is treated with the penalty method, as described in section 2.6. The penalty parameter ε_{n} is increased proportionally to the average element length. Three meshes of increasing refinement are considered, which are summarized together with the penalty parameter in Table 4. The problem was also studied in Corbett and Sauer (2014), where only the enrichment Q1N2 was compared to tri-linear Q1 elements. Here, the Q1N2.1 enrichment with Q1E9 elements in the bulk is considered, which led to very good results in the 2D cases studied in Corbett and Sauer (2014). Also, the results are compared to tri-variate NURBS meshes to investigate the influence of the higher-order bulk integration on the surface quantities. As in the previous example, enhanced assumed strain elements Q1E9 are used for all tri-linear elements to diminish locking effects.

One of the surface quantities of interest is the torque around the z-axis, which should be zero for the frictionless case. For mesh 2, the oscillation of the torque is shown for the meshes with an isogeometric surface in Figure 18a[6]. The periodicity of the resulting torque with a frequency of 90° and the symmetry about 90° are both direct consequences of the smooth surface meshes, which have the same properties with respect to the axis of rotation. In contrast, although the faceted linear meshes are also symmetric, the resulting torque does not inherit this property due to interlocking elements, as has been discussed in Corbett and Sauer (2014). The results obtained with Q1E9+Q1N2 and IGA2 meshes, which both use identical surface meshes in the contact routine, are very similar. This supports the proposition that improving the surface discretization has a large influence on the accuracy of the results, while the bulk discretization is of minor importance in this case. Considering the number of degrees of freedom of mesh 2, the tri-variate NURBS discretization IGA2 has almost 60% more degrees of freedom than the enriched Q1E9+Q1N2 mesh, see Table 4. Concerning efficiency, the contact integrals are identical for both discretizations while the computational cost to evaluate bulk elements is obviously higher for the 27-control-point IGA2 element than for the 8-node Q1E9 element or the 13-node enriched element Q1N2 on the surface.

The values for the Q1E9 elements are omitted in Figure 18a as they are about one order of magnitude larger than those of the meshes with an isogeometric surface representation. This can be seen in Figure 18b, where the convergence of the torque with respect to the number of degrees of freedom is plotted. The convergence rate is the same for all element types, but there is a large difference in the absolute values. In this case, the cubic enrichments Q1E9+Q1N3 and Q1E9+Q1N2.1 are the most accurate.

In contrast to the torque, the contact force does not only depend on the surface deformation, but also on the bulk deformation. As has been shown in the element study in section 4, linear Lagrange elements with and without isogeometric enrichment are rather stiff for coarse

---

[6]The two-half-pass algorithm evaluates the forces separately on each surface. The torque evaluated on the hemisphere is plotted as a solid line, the dashed line corresponds to the cube.
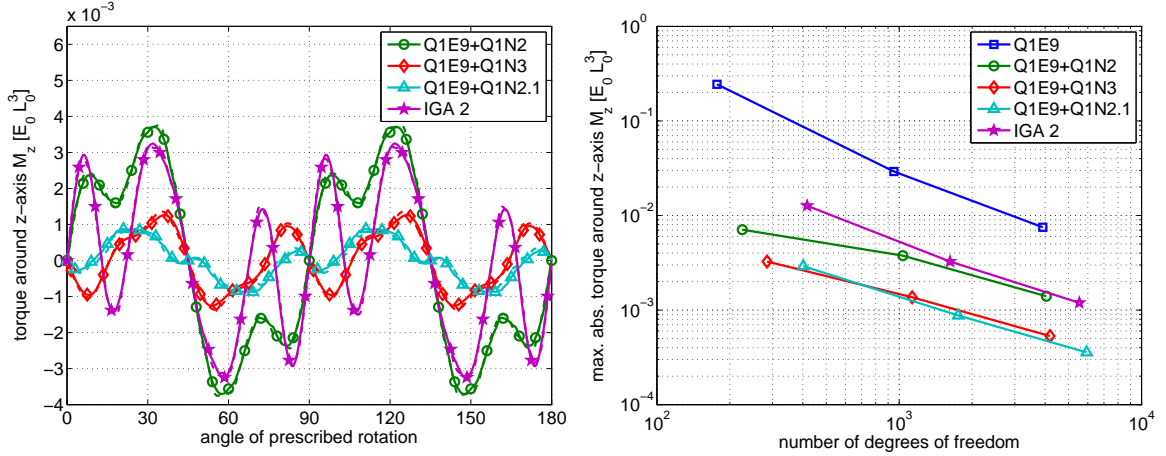
(a) torque for mesh 2, the dashed and the solid lines correspond to the torque evaluated on the cube and on the hemisphere, respectively

(b) convergence with mesh refinement

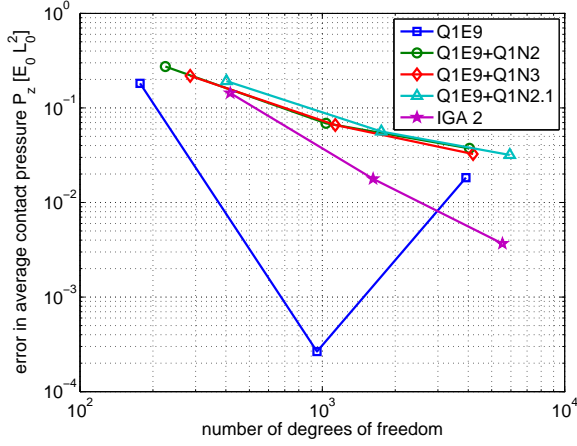Figure 18: Frictionless sliding contact: torque around z-axis.

meshes. Enhanced assumed strain elements (Q1E9) can overcome this, but in the enriched case a layer of isogeometrically enriched elements without the enhancement remains. Due to this, the tri-variate isogeometric discretization converges quicker than the isogeometrically enriched discretizations. Despite using the enhanced assumed strain method, the very poor approximation of the hemisphere's surface with linear elements on coarse meshes together with the limited possibility for the cube's surface to deform accordingly, leads to a very poor computation of the contact forces for Q1E9 elements. This can be seen in Figure 19a, where the average contact force is compared to a reference solution computed with IGA on a fine mesh. The average contact force lies below the reference solution on the coarsest Q1E9 mesh and above the reference value on mesh 3. This pass through the reference value leads to the seemingly small error of the Q1E9 mesh 2 in Figure 19.

Comparing the results for the contact force of the isogeometrically enriched elements with tri-linear Lagrange and tri-variate NURBS discretizations, the enriched elements offer a compromise between both. IGA does deliver better results, but requires 3D meshing which is challenging for general geometries. Using the isogeometric element enrichment, the contact force response is smoother than with a faceted bi-linear surface and converges smoothly, even though the convergence rate is lower than with pure IGA. The use of quadratic Lagrange elements for the bulk and in the enrichment, Q2N2 elements for example, would come at the cost of significantly higher computational effort and do not seem necessary here.
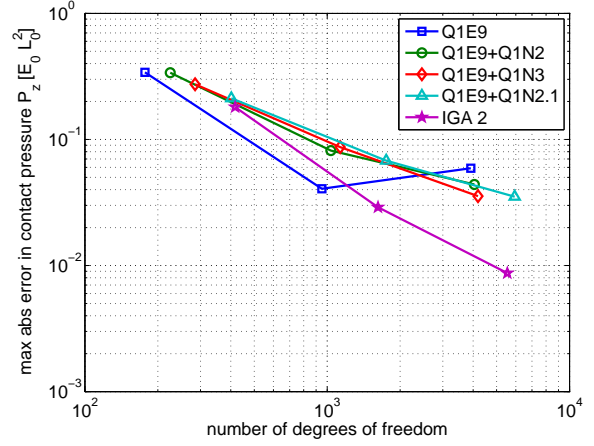
5.3 Frictional sliding contact

The problem set-up is the same as in the previous example, with the exception that frictional contact is considered during the twisting of the hemisphere. During the downward motion the contact remains frictionless. Frictional contact is modeled according to section 2.7 with the tangential penalty parameter $\varepsilon_t = \varepsilon_n$. The element types and discretizations also remain unchanged compared to the frictionless case, summarized in Table 4.

After the downward motion, initially the entire interface is considered to be in a sticking state. As the rotation progresses, the outermost points start to slide, with the sticking–sliding boundary moving inward with increasing rotation. After approximately 120° all integration points on
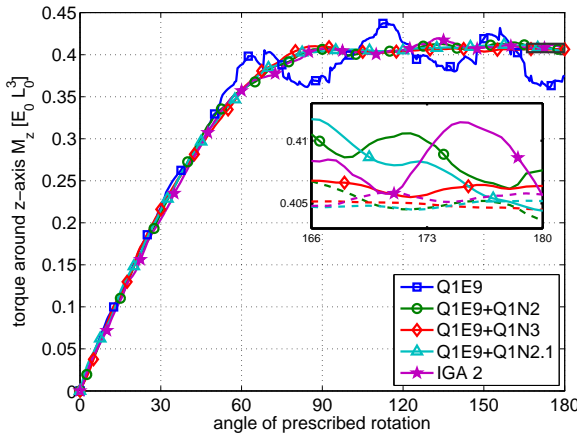
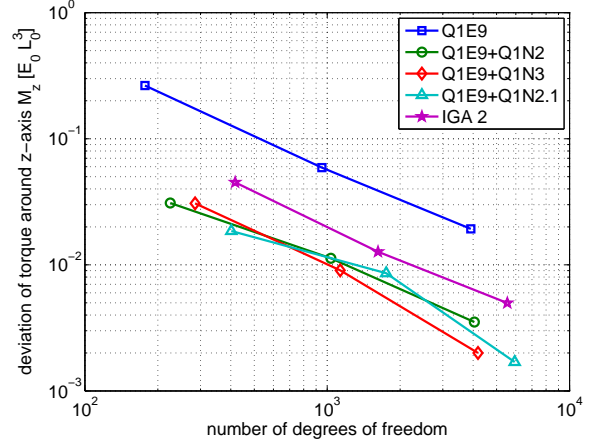(a) Error in average contact force.

(b) Maximum error in contact force.

Figure 19: Frictionless sliding contact: convergence of contact force w.r.t. the reference solution.

(a) Torque for mesh 2.

(b) Convergence with mesh refinement.

Figure 20: Frictional sliding contact: torque around z-axis.

both surfaces are sliding. Up to this point the torque around the z-axis increases continuously and upon reaching the sliding state should remain at this maximum value for the rest of the computation. This is shown in Figure 20a for mesh 2. The faceted surfaces of the Q1E9 mesh clearly lead to poorer results than the smooth surfaces discretized with isogeometric basis functions. The large oscillation of the torque for Q1E9 elements is due to interlocking of elements. Eventually, these elements separate and spring back. This large relative tangential motion between two surface points is challenging for frictionless contact. For frictional contact it becomes even more challenging, as friction is path-dependent and relies on the accurate computation of the tangential slip.

As has been shown in the previous example 5.2, the computed contact force P_z is less accurate for Q1E9 elements and enriched elements than for the tri-variate isogeometric discretization. The frictional traction depends directly on the normal contact pressure, see section 2.7. This means that while the oscillation of the torque value can be decreased with the isogeometric element enrichment, the convergence of the absolute value depends on the bulk reaction as well as the surface. In Figure 20b the maximum deviation of the torque with respect to the

elements	max($\|t_x\|$)	
	$\in \partial_e \mathcal{B}_1$	$\in \partial_e \mathcal{B}_2$
Q1E9	0.296	0.175
IGA2	0.217	0.175
Q1E9+Q1N2	0.235	0.177
Q1E9+Q1N3	0.183	0.148
Q1E9+Q1N2.1	0.280	0.237
reference	0.292	0.291

Table 5: Maximum absolute value of the tangential traction component t_x on mesh 2.

average torque between $120°$ and $180°$ of the respective mesh is plotted over the number of degrees of freedom. This shows the reduction of the torque's oscillation with increasing mesh refinement, independent of the absolute, pressure-dependent value of the torque. With respect to the absolute value, the behavior is comparable to the convergence of the contact force in the previous example.

Besides evaluating the global response, one can also examine local effects. Friction leads to tangential traction on the contact surfaces, depicted in Figure 21 after a frictional rotation of $180°$. The tangential traction component $t_x = \boldsymbol{t}_t \cdot \boldsymbol{e}_x$ is plotted in a top-down view on the deformed surfaces $\partial_e \mathcal{B}_k$, which have been moved apart for visibility. The post-processing scheme proposed in Sauer (2013) is applied to the raw traction data given at the quadrature points, leading to a smooth distribution. Figure 21f shows the solution on a fine mesh, computed with Q1E9+Q1N2.1 elements which is used as reference, while the other results are obtained on mesh 2. The poor approximation of both, the deformation and the traction field t_x, by the Q1E9 mesh in Figure 21a is clearly visible. Figures 21b to 21e show surfaces discretized by isogeometric basis functions. Compared to the reference solution, the deformation field is in good agreement.

However, the traction field still shows large differences, with respect to both the maximum value and the contours. Increasing surface continuity leads to increasing smoothing of the results, as can be seen in the difference between Figure 21c and 21d for the Q1N2 and Q1N3 surface meshes. The sharp boundary between the surface in contact $\partial_c \mathcal{B}_k$ and the rest of the surface is not represented well by these meshes and the peak value becomes smaller as the traction field is smoothed. The best result in terms of the traction field is obtained by the Q1E9+Q1N2.1 mesh. The reduced basis span and increased number of degrees of freedom on the surface lead to a good approximation of the traction field even on a coarse mesh.

The maximum traction values are summarized in Table 5 and support the effects described above. Interlocking of elements leads to spurious tangential tractions on the faceted Q1E9 surface and the seemingly good result on the hemisphere.

In summary, the isogeometric element enrichment makes the computation more robust due to the lack of interlocking elements, simplifies contact treatment as no corner or edge contact occurs, and leads to less oscillation in the reaction forces. These benefits can also be obtained with a purely isogeometric mesh, however on more complex geometries the enrichment has the advantage of simpler mesh generation. Concerning the global response, the linear Lagrange element that the enriched elements are based on can lead to slower convergence than in the purely isogeometric case. A solution is to use the computationally more expensive isogeometrically enriched elements based on quadratic Lagrange elements. Locally the enrichment has the advantage that a surface discretization with many degrees of freedom, such as Q1N2.1, can be used without increasing the number of degrees of freedom in the rest of the body, as it would
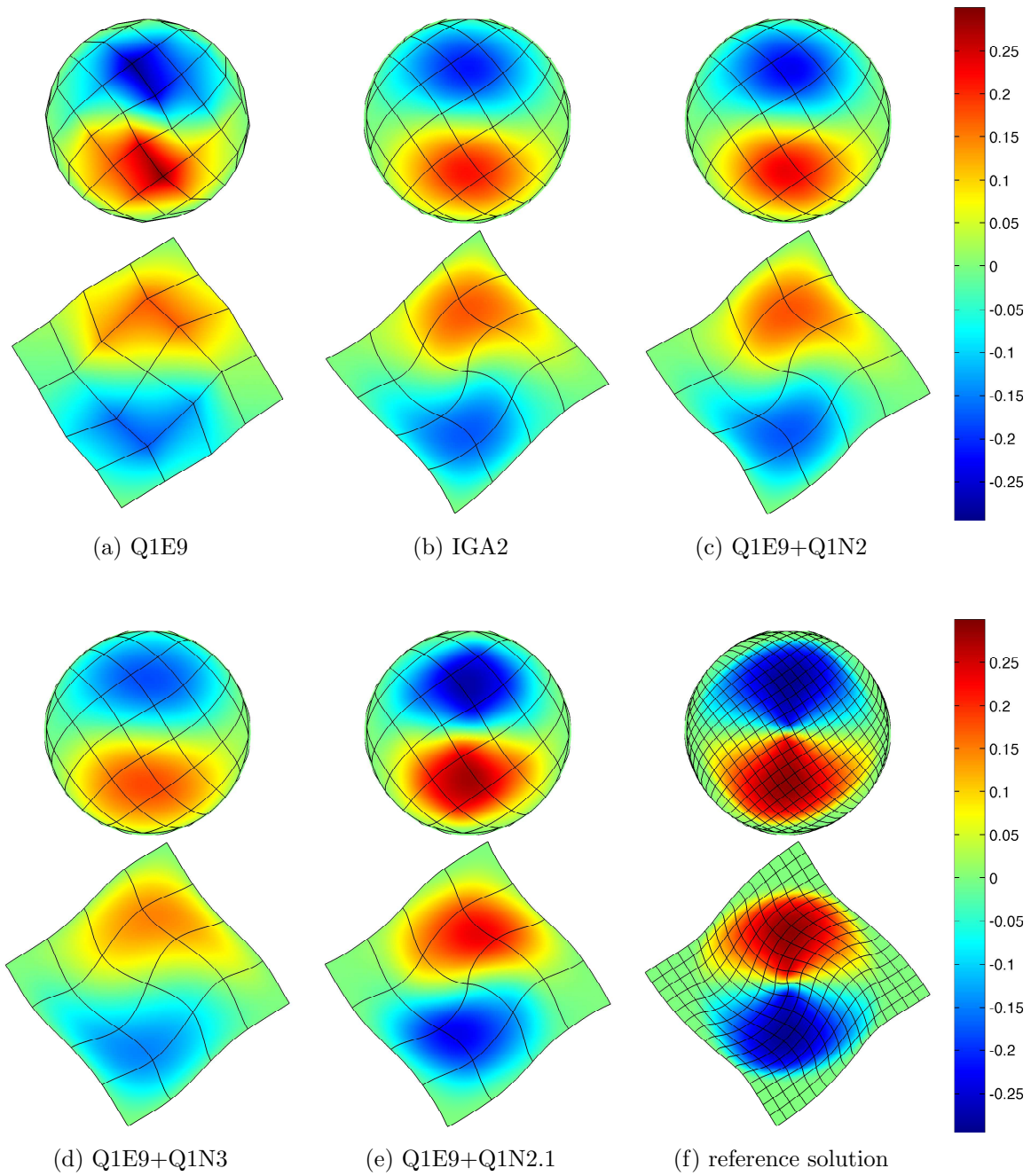
Figure 21: Frictional sliding contact: top–down view of tangential contact traction component $t_x = \boldsymbol{t}_t \cdot \boldsymbol{e}_x$ after rotation of $180°$ for mesh 2. For visibility, only the deformed surfaces $\partial_e \mathcal{B}_k$ are shown and have been moved apart. The traction is smoothed according to the post-processing scheme proposed in Sauer (2013).

be the case with a pure IGA mesh. The advantage of higher accuracy on the surface has been shown in the case of the tangential traction field.

6 Conclusion

Several new aspects of isogeometrically enriched elements, introduced in section 2, have been analyzed and discussed in this work. The element study in section 4 shows that the enriched elements converge to the correct solution with increasing mesh refinement. Even if no surface effects are present and only volume integrals are solved in the computation, enriched linear Lagrange finite elements (Q1N2) lead to more accurate results on coarse meshes than standard tri-linear elements (Q1). In the example in section 4.3 the relative error in the reaction force could be reduced by a factor of 3.

In the case of compression, enhanced assumed strain elements (Q1E9) lead to very good results. No such enhancement has been developed yet in conjunction with the enrichment technique, so that the enriched layer on the surface is currently still based on linear Lagrange elements. The development of an isogeometrically enriched enhanced assumed strain element, Q1E9Np, seems promising and remains a topic for future research. Good results are also achieved by enriched quadratic Lagrange elements (Q2N2), but the gain over standard quadratic Lagrange elements (Q2) in problems that do not require surface continuity is negligible. We do note however, that the presented enrichment technique only requires an isogeometric surface mesh and allows volumetric meshing of arbitrary geometries, as is demonstrated in section 3. A layer of enriched hexahedral elements on the surface can be combined with arbitrary elements in the bulk, including hexahedra, tetrahedra, prisms and pyramids.

The numerical examples in section 5 show that for problems dominated by effects on the surface or where surface quantities are of interest, the enrichment technique offers high accuracy at low additional computational cost. Continuity of C^1 or higher can be achieved across element boundaries and the number of degrees of freedom on the surface can be increased by means of order elevation without changing the bulk mesh.

Summarizing the results, one can say that the enrichment technique offers benefits for general problems, especially on coarse meshes and problems with large deformations, see Figure 12. Its major benefit lies in solving surface-dominated problems. Here, the higher continuity and order of interpolation on the surface combined with computationally inexpensive and simple Lagrange elements in the bulk offer a great advantage over other methods. A current drawback of the enrichment technique with linear Lagrange elements is that the elements can show the same shear locking behavior as tri-linear elements. To overcome this, quadratic Lagrange elements can be used as base for the enrichment. It is emphasized that the locking is not a consequence of the enrichment but comes from the underlying linear interpolation. In future research, the development of locking-free enriched elements could lead to a more efficient treatment of these cases.

Finally, the proposed elements are also expected to behave advantageously when applied to other physical problems, like fluid-structure interaction, free-surface flow, electrostatic and electromagnetic interaction, or acoustics.

References

Bommes, D., Campen, M., Ebke, H.-C., Alliez, P., and Kobbelt, L. (2013). Integer-grid maps for reliable quad meshing. *ACM Trans. Graph.*, **32**(4):98:1–98:12.

Borden, M. J., Scott, M. A., Evans, J. A., and Hughes, T. J. R. (2011). Isogeometric finite element data structures based on bezier extraction of NURBS. *Int. J. Numer. Meth. Engng.*, **87**:15–47.

Corbett, C. J. and Sauer, R. A. (2014). Nurbs-enriched contact finite elements. *Comput. Methods Appl. Mech. Engrg.*, **275**:55–75.

Cottrell, J. A., Hughes, T. J. R., and Bazilevs, Y. (2009). *Isogeometric Analysis*. Wiley.

Crisfield, M. A. and Alfano, G. (2002). Adaptive hierarchical enrichment for delamination fracture using a decohesive zone model. *Int. J. Numer. Meth. Engrg.*, **54**(9):1369–1390.

De Lorenzis, L., Evans, J. A., Hughes, T. J. R., and Reali, A. (2015). Isogeometric collocation: Neumann boundary conditions and contact. *Comput. Methods Appl. Mech. Engrg.*, **284**:21–54.

Dimitri, R., De Lorenzis, L., Scott, M. A., Wriggers, P., Taylor, R. L., and Zavarise, G. (2014a). Isogeometric large deformation frictionless contact using T-splines. *Comput. Methods Appl. Mech. Engrg.*, **269**:394–414.

Dimitri, R., De Lorenzis, L., Wriggers, P., and Zavarise, G. (2014b). NURBS- and T-spline-based isogeometric cohesive zone modeling of interface debonding. *Comput. Mech.*, **54**:369–388.

Dittmann, M., Franke, M., Temizer, I., and Hesch, C. (2014). Isogeometric Analysis and thermomechanical Mortar contact problems. *Comput. Methods Appl. Mech. Engrg.*, **274**:192–212.

Escobar, J. M., Cascon, J. M., Rodriguez, E., and Montenegro, R. (2011). A new approach to solid modeling with trivariate T-splines based on mesh optimization. *Comput. Methods Appl. Mech. Engrg.*, **200**(45-46):3210–3222.

Hughes, T., Cottrell, J., and Bazilevs, Y. (2005). Isogeometric analysis: CAD, finite elements, NURBS, exact geometry and mesh refinement. *Comp. Meth. Appl. Mech. Engrg.*, **194**:4135–4195.

Laursen, T. A. (2002). *Computational Contact and Impact Mechanics: Fundamentals of modeling interfacial phenomena in nonlinear finite element analysis*. Springer.

Liu, L., Zhang, Y., Hughes, T., Scott, M., and Sederberg, T. (2014). Volumetric T-spline construction using boolean operations. *Eng. Comput.*, **30**(4):425–439.

Sauer, R. A. (2011). Enriched contact finite elements for stable peeling computations. *Int. J. Numer. Meth. Engrg.*, **87**:593–616.

Sauer, R. A. (2013). Local finite element enrichment strategies for 2D contact computations and a corresponding postprocessing scheme. *Comput. Mech.*, **52**:301–319.

Sauer, R. A. (2014). Stabilized finite element formulations for liquid membranes and their application to droplet contact. *Int. J. Numer. Methods Fluids*, **75**:519–545.

Sauer, R. A. and De Lorenzis, L. (2013). A computational contact formulation based on surface potentials. *Comput. Methods Appl. Mech. Engrg.*, **253**:369–395.

Sauer, R. A. and De Lorenzis, L. (2014). An unbiased computational contact formulation for 3D friction. *Int. J. Numer. Meth. Engng.*, in press (http://dx.doi.org/10.1002/nme.4794).

Sauer, R. A., Duong, T. X., and Corbett, C. J. (2014). A computational formulation for constrained solid and liquid membranes considering isogeometric finite elements. *Comput. Methods Appl. Mech. Engrg.*, **271**:48–68.

Schillinger, D., Dede, L., Scott, M. A., Evans, J. A., Borden, M. J., Rank, E., and Hughes, T. J. R. (2012). An isogeometric design-through-analysis methodology based on adaptive hierarchical refinement of nurbs, immersed boundary methods, and t-spline cad surfaces. *Comput. Methods Appl. Mech. Engrg.*, **249**:116–150.

Scott, M. A., Borden, M. J., Verhoosel, C. V., Sederberg, T. W., and Hughes, T. J. R. (2011). Isogeometric finite element data structures based on Bézier extraction of T-splines. *Int. J. Numer. Meth. Engng.*, **88**(2):126–156.

Simo, J. C. and Armero, F. (1992). Geometrically non-linear enhanced strain mixed methods and the method of incompatible modes. *Int. J. Numer. Meth. Engng.*, **33**:1413–1449.

Stupkiewicz, S. (2001). Extension of the node-to-segment contact element for surface-expansion-dependent contact laws. *Int. J. Numer. Meth. Engng.*, **50**(3):739–759.

Temizer, I. (2014). Multiscale thermomechanical contact: Computational homogenization with isogeometric analysis. *Int. J. Numer. Meth. Engrg.*, **97**(8):582–607.

Verhoosel, C. V., Scott, M. A., de Borst, R., and Hughes, T. J. R. (2011). An isogeometric approach to cohesive zone modeling. *Int. J. Numer. Meth. Engng.*, **87**:336–360.

Wang, W., Zhang, Y., Liu, L., and Hughes, T. (2013). Trivariate solid T-spline construction from boundary triangulations with arbitrary genus topology. *Comput. Aided Des.*, **45**(2):351–360.

Wriggers, P. (2006). *Computational Contact Mechanics*. Springer, 2nd edition.

Wriggers, P. (2008). *Nonlinear Finite Element Methods*. Springer.

Xu, X.-P. and Needleman, A. (1993). Void nucleation by inclusion debonding in a crystal matrix. *Model. Simul. Mater. Sci. Engng.*, **1**(2):111–132.

Zhang, Y., Wang, W., and Hughes, T. J. (2012). Solid T-spline construction from boundary representations for genus-zero geometry. *Comput. Meth. Appl. Mech. Engrg.*, **249-252**:185–197.

Zienkiewicz, O. C. and Taylor, R. L. (2005). *The Finite Element Method for Solid and Structural Mechanics*. Butterworth-Heinemann, 6th edition.